



# Design of improved CoMo hydrotreating catalyst via engineering of carbon nanotubes@alumina composite support

Mariya A. Kazakova<sup>a,b,\*</sup>, Yulia V. Vatutina<sup>a</sup>, Alexander G. Selyutin<sup>b,c</sup>, Igor P. Prosvirin<sup>a</sup>, Evgeniy Yu. Gerasimov<sup>a,b</sup>, Oleg V. Klimov<sup>a</sup>, Alexander S. Noskov<sup>a</sup>, Maxim O. Kazakov<sup>a,b</sup>

<sup>a</sup> Borekov Institute of Catalysis SB RAS, Novosibirsk 630090, Russia

<sup>b</sup> Novosibirsk State University, Pirogova 2, Novosibirsk 630090, Russia

<sup>c</sup> Synchrotron radiation facility SKIF, Borekov Institute of Catalysis SB RAS, Nikol'skiy Prospekt 1, Kol'tsovo 630559, Russia

## ARTICLE INFO

### Keywords:

CoMo catalyst  
Multi-walled carbon nanotubes  
Alumina  
Composite support  
Hydrotreating

## ABSTRACT

An efficient strategy for the synthesis of nanostructured composite supports for CoMoS hydrotreating catalysts has been proposed. The synthesis concept is based on the growth of multi-walled carbon nanotubes (MWCNTs) on alumina crystallites modified with Fe<sub>2</sub>Co nanoparticles. The morphology and structural characteristics of the obtained MWCNT@Al<sub>2</sub>O<sub>3</sub> supports were tuned by varying Fe<sub>2</sub>Co content. A comprehensive analysis using advanced techniques revealed the optimal content and structural characteristics of MWCNTs in composite supports that positively affect the morphology of the sulfide component. It has been established that for the best CoMoS/MWCNT@Al<sub>2</sub>O<sub>3</sub> catalyst, which is characterized by the highest dispersion of sulfide component and CoMoS phase content, the activity in dibenzothiophene hydrodesulfurization and quinoline hydrogenation significantly exceeds the activity of CoMoS/Al<sub>2</sub>O<sub>3</sub> and CoMoS/MWCNT catalysts. The proposed approach can be applied to improve the activity of both conventionally used hydrotreating catalysts and catalysts for other practically important processes by carefully tuning metal-support interaction.

## 1. Introduction

Numerous attempts to improve conventional hydrotreating catalysts are largely undertaken due to the growing demand for high-quality ultra-clean fuels as well as strict environmental regulations [1]. Typical hydrotreating catalysts are Co(Ni)Mo sulfides supported on alumina [2]. It has been reliably established that the support significantly affects the activity and stability of hydrotreating catalysts. Namely, the nature of the support determines the composition, dispersion, and morphology of the active sulfide component [3,4]. It is known that gamma alumina, due to such characteristics as appropriate textural properties, thermal stability, high mechanical strength, and availability is widely used for commercial hydrotreating catalysts preparation. However, the strong interaction between the active component precursors and alumina support leads to the partial formation of the species, which are difficult to reduce and sulfide, thus leading to a decrease in the activity of hydrotreating catalysts [3]. In addition, strong acid sites of the alumina surface may promote undesirable reactions with heavy feedstock components leading to enhanced coke formation and

deactivation. In this regard, the scientific community pays great attention to enhancing the performance of conventional hydrotreating catalysts by improving the support properties. The literature presents studies of various materials as potential supports for hydrotreating catalysts, such as metal oxides (ZrO<sub>2</sub> [5], TiO<sub>2</sub> [6], SiO<sub>2</sub> [7]), ordered mesoporous silica materials [8,9], zeolites [10], as well as carbon materials of different nature, including activated carbon [9], macroporous and mesomacroporous carbon [11], carbon nanotubes [12–14], carbon nanofibers [15]. Among the presented supports, carbon materials attract special attention due to their outstanding textural and structural characteristics, as well as low acidity, which limits the formation of condensation products during hydrotreating reactions [16]. However, the main limitation for the practical use of pure carbon materials as hydrotreating catalysts support, which is usually not considered in scientific publications, is associated with the difficulties in preparing the granules of a required shape and mechanical strength. In addition, activated carbon supports are characterized by microporosity, which hinders the diffusion of bulk molecules and complicates the conversion of heavy feedstocks. Recently, considerable attention has been focused

\* Corresponding author at: Borekov Institute of Catalysis SB RAS, Novosibirsk 630090, Russia.

E-mail address: [mas@catalysis.ru](mailto:mas@catalysis.ru) (M.A. Kazakova).

<https://doi.org/10.1016/j.apcatb.2023.122475>

Received 20 November 2022; Received in revised form 10 January 2023; Accepted 15 February 2023

Available online 16 February 2023

0926-3373/© 2023 Elsevier B.V. All rights reserved.

on the development of composite supports for hydrotreating catalysts. The main task in the synthesis of such materials is to combine the positive characteristics of the various components. The appropriate combination will result in the formation of a new material with improved properties, namely optimal acidity and reduced metal-support interaction required to obtain a high-active Co(Ni)MoS type II phase [17]. It should be noted that when developing composite support, the choice of the components nature, their ratio, as well as the preparation method is of decisive importance. The approaches presented in the literature can be divided into three groups. The first one includes composite supports obtained by combining two oxide components characterized by different acidic properties, including  $\text{TiO}_2\text{-Al}_2\text{O}_3$  [18],  $\text{Al}_2\text{O}_3\text{-SiO}_2$  [19],  $\text{TiO}_2\text{-ZrO}_2$  [20],  $\text{TiO}_2\text{-SiO}_2$  [21], MCM-41- $\text{Al}_2\text{O}_3$  [22], and others. The next approach is to combine oxide components of acidic and basic nature, for example,  $\text{Al}_2\text{O}_3\text{-MgO}$  [18],  $\text{TiO}_2\text{-MgO}$  [23],  $\text{Al}_2\text{O}_3\text{-TiO}_2\text{-MgO}$  [24]. The third approach is to combine an oxide component having acidic nature with naturally neutral carbon materials. Composite materials based on alumina-carbon [25–27], alumina-carbon nanofiber [28], alumina-graphene [29], alumina-carbon nanotube [30], zeolite-carbon [31], zeolite-carbon nanofiber [32] are among such systems. Currently, the combination of supports based on alumina and carbon materials is attracting more and more attention. This is primarily because each of these components has its advantages when used as a support for hydrotreating catalyst. Whereas the effective design of composite support based on these materials will allow the combination of each component positive characteristics and overcome their individual drawbacks. Among the wide variety of carbon materials, multi-walled carbon nanotubes (MWCNTs) are of considerable interest, primarily because their morphology and structural characteristics can be easily tuned by choosing a catalyst for their growth, as well as by varying the synthesis conditions [33]. MWCNTs can be prepared with the controlled pore volume and size without microporosity, and their structure can be modified with various functional groups [34,35]. In addition, it is well known that the presence of nitrogen-containing compounds in the feedstock has a strong inhibitory effect on the hydrodesulfurization reactions due to the competitive adsorption of S- and N-containing compounds on the same active sites [8,17]. However, this inhibition can be diminished by increasing the hydrogenation activity of the catalyst [36]. Highly defective MWCNTs characterized by a low degree of crystallinity have an increased ability to adsorb hydrogen and a good interfacial diffusion of adsorbed hydrogen atoms (H-spillover) [37]. Thus, a properly organized MWCNT structure in the support can act as a hydrogen transfer agent during the H-spillover from the active sites to the adsorbed feedstock molecules, increasing hydrodesulfurization and hydrogenation activity.

In the framework of this study, an efficient strategy for the synthesis of a nanostructured mesoporous MWCNT@ $\text{Al}_2\text{O}_3$  composite support for a CoMoS hydrotreating catalyst was proposed. This strategy is based on the MWCNTs growth directly on alumina crystallites by chemical vapor decomposition (CVD) of ethylene on the surface of alumina granules modified by  $\text{Fe}_2\text{Co}$  alloy nanoparticles. Here we discuss the importance of fine-tuning the composition, morphology, and structural-textural characteristics of MWCNT@ $\text{Al}_2\text{O}_3$  supports for the formation of active CoMoS phase. The advantages of the proposed strategy were demonstrated by comparing the catalytic activity of CoMoS/MWCNT@ $\text{Al}_2\text{O}_3$  with CoMoS/MWCNT and CoMoS/ $\text{Al}_2\text{O}_3$  catalysts in dibenzothiophene hydrodesulfurization and quinoline hydrodenitrogenation.

## 2. Experimental

### 2.1. Preparation of MWCNT@ $\text{Al}_2\text{O}_3$ supports

At the first stage of composite supports preparation, the initial  $\gamma\text{-Al}_2\text{O}_3$  sample was obtained from a commercial boehmite powder (HQ 102 B, Hebei Easttree Industrial Co., China) by molding [25]. An aqueous solution of ammonia (Reachim Ltd.) was used as a plasticizing

agent ( $\text{NH}_3/\text{Al}_2\text{O}_3$  molar ratio of 0.09). The obtained sample was dried at 110 °C for 2 h and calcined at 700 °C for 4 h in an air stream. Then, calcined alumina granules were crushed and sieved to obtain an alumina support sample with a particle size of 0.25–0.5 mm. The calcination temperature of 700 °C was chosen to avoid possible phase transitions and changes in the textural characteristics of alumina during the further synthesis of composite supports.

At the second stage of the MWCNT@ $\text{Al}_2\text{O}_3$  composite supports synthesis  $\text{Fe}_2\text{Co}$  active component of the MWCNT growth catalyst was loaded into  $\gamma\text{-Al}_2\text{O}_3$  sample by incipient wetness impregnation with mixed aqueous solutions of iron (III) nitrate (Sigma-Aldrich) and cobalt (II) nitrate (Sigma-Aldrich) ( $\text{Fe}:\text{Co}$  molar ratio of 2:1). The concentrations of impregnation solutions were chosen to vary the content of  $\text{Fe}_2\text{Co}$  from 0.5 to 10 wt%. The composition of the  $\text{Fe}_2\text{Co}$  active component was chosen since earlier catalysts based on it demonstrated high performance in the MWCNT synthesis reaction and also contributed to the growth of nanotubes with a narrow diameter distribution and low defectiveness [38,39]. The obtained x%  $\text{Fe}_2\text{Co}/\text{Al}_2\text{O}_3$  samples were dried at 110 °C for 4 h and calcined at 350 °C for 4 h in an air stream. Synthesis of MWCNTs on the surface of x%  $\text{Fe}_2\text{Co}/\text{Al}_2\text{O}_3$  samples was carried out by ethylene CVD at a temperature of 680 °C for 15 min under conditions similar to the MWCNT synthesis reaction ( $\text{C}_2\text{H}_4:\text{Ar} = 1:1$ , flow rate of 400 ml/min) [38,39]. The obtained composite supports were denoted as MWCNT(x%  $\text{Fe}_2\text{Co}$ )@ $\text{Al}_2\text{O}_3$ , where x% is the content of the active component for MWCNT growth.

### 2.2. CoMoS catalysts preparation

CoMo catalysts were prepared by impregnation of  $\gamma\text{-Al}_2\text{O}_3$ , MWCNT (the sample is similar to the sample used earlier in [13]), and MWCNT(x%  $\text{Fe}_2\text{Co}$ )@ $\text{Al}_2\text{O}_3$  supports with aqueous solutions containing cobalt (II) carbonate hydrate (Sigma-Aldrich) and ammonium heptamolybdate (Sigma-Aldrich) as active component precursors and citric acid (Reachim Ltd.) as a chelating agent. More details on the catalyst synthesis procedure are described in [13]. Impregnation solution concentrations were chosen so that the content of Co and Mo in the catalysts was 3.2 and 12.0 wt%, respectively. The obtained catalyst samples were dried at 120 °C for 4 h in an air stream. The catalysts were sulfided in a pure  $\text{H}_2\text{S}$  flow (flow rate of 5 ml/min per 1 g of the catalyst) at atmospheric pressure for 2 h at a temperature of 220 °C and 2 h at a temperature of 400 °C. After the completion of the sulfidation, the  $\text{H}_2\text{S}$  flow at 400 °C was switched to an Ar flow (5 ml/min per 1 g of the catalyst), and the catalyst was cooled to room temperature. Then one part of the catalyst was immediately loaded in the reactor for catalytic testing, and another part was collected and placed in hexane to prevent it from contact with air before further characterization. The obtained sulfide catalysts were denoted as CoMoS/ $\text{Al}_2\text{O}_3$ , CoMoS/MWCNT, and CoMoS/MWCNT(x%  $\text{Fe}_2\text{Co}$ )@ $\text{Al}_2\text{O}_3$ , where x% is the  $\text{Fe}_2\text{Co}$  content of the active component for MWCNT growth.

### 2.3. Supports and catalysts characterization

#### 2.3.1. X-ray diffraction (XRD)

The phase composition of the x%  $\text{Fe}_2\text{Co}/\text{Al}_2\text{O}_3$  catalysts for MWCNT growth, as well as the MWCNT(x%  $\text{Fe}_2\text{Co}$ )@ $\text{Al}_2\text{O}_3$  composite supports, was studied using an ARL X'TRA (Thermo Electron Corporation) diffractometer, equipped with a vertical theta geometry (Bragg–Brentano), CuK $\alpha$  radiation ( $\lambda = 0.15418$  nm) and a Peltier cooled Si(Li) solid-state detector. X-ray patterns were recorded in  $2\theta$  angles range from 18° to 70° with a step of 0.05° and a counting time of 3 s. The phase analysis of X-ray patterns was carried out using the PDF-2 database. Quantitative analysis of X-ray patterns was carried out using the Fityk program. The sizes of coherent scattering region (CSR) were calculated using the Scherrer equation.

### 2.3.2. Raman spectroscopy

Structural characteristics and defectiveness of MWCNT in MWCNT(x% Fe<sub>2</sub>Co)@Al<sub>2</sub>O<sub>3</sub> supports were evaluated using Raman spectroscopy on a LabRAM HR Evolution spectrometer (Horiba) and Ar laser radiation with a wavelength of 514.5 nm.

### 2.3.3. CHNS analysis

The total carbon content in the MWCNT(x% Fe<sub>2</sub>Co)@Al<sub>2</sub>O<sub>3</sub> supports was determined on a EuroEA3000 CHNS automatic analyzer (Euro-Vector S.p.A.).

### 2.3.4. Scanning electron microscopy (SEM)

The morphology of the MWCNT(x% Fe<sub>2</sub>Co)@Al<sub>2</sub>O<sub>3</sub> supports was studied using a JSM-6460LV scanning electron microscope (JEOL Ltd.) with an accelerating voltage of 16–19 kV.

### 2.3.5. X-ray fluorescence (XRF)

The elemental composition of MWCNT(x% Fe<sub>2</sub>Co)@Al<sub>2</sub>O<sub>3</sub> supports and CoMoS/MWCNT(x% Fe<sub>2</sub>Co)@Al<sub>2</sub>O<sub>3</sub> catalysts was studied on an ARL Perform X analyzer with an X-ray tube Rh anode. In more detail, the analysis procedure is described in [40].

### 2.3.6. Nitrogen adsorption-desorption

The textural characteristics of MWCNT(x% Fe<sub>2</sub>Co)@Al<sub>2</sub>O<sub>3</sub> supports and CoMoS/MWCNT(x% Fe<sub>2</sub>Co)@Al<sub>2</sub>O<sub>3</sub> catalysts were studied by low-temperature nitrogen adsorption using an ASAP 2400 instrument (Micrometrics). Before measurement, the samples were degassed in a vacuum at 150 °C. The specific surface area (*S*<sub>BET</sub>, m<sup>2</sup>/g) was calculated by the BET equation from nitrogen adsorption at relative pressures in the range from 0.05 to 0.30. The total pore volume was determined from the amount of nitrogen adsorbed at a relative pressure close to unity by applying the Gurvich rule. The pore size distribution was calculated using the BJH method for the desorption branch of the isotherm.

### 2.3.7. Transmission electron microscopy (TEM)

The structural characteristics of MWCNT(x% Fe<sub>2</sub>Co)@Al<sub>2</sub>O<sub>3</sub> composite supports and the morphology of CoMoS/MWCNT(x% Fe<sub>2</sub>Co)@Al<sub>2</sub>O<sub>3</sub> catalysts were studied using a JEM-2010 transmission electron microscope (JEOL Ltd.) operating at an accelerating voltage of 200 kV, which provides a nominal resolution of 0.14 nm. The distribution of MWCNTs diameters in MWCNT(x% Fe<sub>2</sub>Co)@Al<sub>2</sub>O<sub>3</sub> was estimated using TEM images of composite supports obtained at × 50000 and × 400000 magnifications containing about 200–400 MWCNTs. At least 15 representative high-resolution micrographs were used to estimate the morphology of sulfide particles. The average slab length and stacking number were calculated for 300–500 slabs located in different areas of each catalyst. MoS<sub>2</sub> dispersion was statistically estimated by the ratio of edge and corner Mo atoms to the total number of Mo atoms in the slab using the average slab length obtained from HRTEM images. The average fraction of the edge and corner Mo atoms was estimated according to [41], assuming that MoS<sub>2</sub> slabs are represented as perfect hexagons. The number of Mo atoms on the edges (*M*<sub>e</sub>) was calculated from Eq1:

$$M_e = \sum_{i=1...t} (6n_i - 12) \quad (1)$$

where *t* is the total number of slabs obtained from HRTEM images; *n<sub>i</sub>* is the number of Mo atoms along one side of the MoS<sub>2</sub> slab, which was determined from the average length of MoS<sub>2</sub> slab  $n_i = \frac{5 \cdot L(\text{nm})}{3.2} + 0.5$  [41].

The number of Mo atoms in the corners (*M*<sub>c</sub>) was calculated from Eq2:

$$M_c = \sum_{i=1...t} 6 \quad (2)$$

The total number of Mo atoms (*M*<sub>T</sub>) was calculated from Eq3:

$$M_T = \sum_{i=1...t} (3n_i^2 - 3n_i + 1) \quad (3)$$

The dispersion of MoS<sub>2</sub> (*f*<sub>Mo</sub>) was calculated from Eq4:

$$f_{Mo} = \sum_{i=1...t} (6n_i - 6) / \sum_{i=1...t} (3n_i^2 - 3n_i + 1) \quad (4)$$

### 2.3.8. X-ray photoelectron spectroscopy (XPS)

The electronic state of the elements in the MWCNT(x% Fe<sub>2</sub>Co)@Al<sub>2</sub>O<sub>3</sub> supports and CoMoS/MWCNT(x% Fe<sub>2</sub>Co)@Al<sub>2</sub>O<sub>3</sub> catalysts was studied using a SPECS photoelectron spectrometer with a PHOIBOS-150 hemispherical energy analyzer and AlK<sub>α</sub> irradiation (*hν* = 1486.6 eV, 200 W). The binding energy scale was preliminarily calibrated using the positions of the peaks of Au4f7/2 (84.0 eV) and Cu2p3/2 (932.7 eV) core levels. The samples were supported with conductive double-sided copper scotch. The C1s peak line (EB = 284.5 eV) was used as an internal reference to correctly calibrate the photoelectron peaks of MWCNT and MWCNT(x% Fe<sub>2</sub>Co)@Al<sub>2</sub>O<sub>3</sub> composite supports, as well as CoMoS catalysts. A low-energy electron gun (FG-15/40, SPECS) was used to neutralize the sample charge.

### 2.4. Hydrotreating activity testing

The catalytic testing of CoMoS catalysts in hydrodesulfurization (HDS) of dibenzothiophene (DBT) (Acros Organics) and hydrodenitrogenation (HDN) of quinoline (Reachim Ltd.) was carried out using a model feedstock containing 1.5 wt% of DBT and 0.1 wt% of quinoline in undecane (Reachim Ltd.). The catalyst sample (0.3 g), pre-sulfided in H<sub>2</sub>S, was mixed with silicon carbide and loaded into the reactor. The experiments were carried out in a fixed bed flow reactor at a temperature of 270 °C, a pressure of 3.5 MPa, a weight hourly space velocity of 20.0 h<sup>-1</sup>, and an H<sub>2</sub>/feedstock volume ratio of 500. Reaction products were analyzed by gas chromatography on a Clarus 580 GC instrument (Perkin Elmer) with a flame ionization detector and capillary column Restek Rtx-DHA-100. Nitrogen content in the feedstock and reaction products was determined using a TE Instruments XPLOER S/N analyzer. The HDS activity of CoMoS catalysts was evaluated by DBT conversion. The HDN activity was assessed by the degree of nitrogen removal from the feedstock (the HDN degree calculated as a relative decrease in the nitrogen content in the products compared to the nitrogen content in the feedstock).

## 3. Results and discussion

### 3.1. Synthesis and characterization of MWCNT@Al<sub>2</sub>O<sub>3</sub> composite supports

To obtain MWCNT@Al<sub>2</sub>O<sub>3</sub> supports, alumina was initially modified with various amounts of MWCNT growth catalyst, followed by the synthesis of nanotubes on the surface of alumina crystallites. Based on the previous studies [39] on the effect of the catalyst active component composition on the activity in the MWCNT growth reaction, as well as the structural characteristics and defectiveness of MWCNTs synthesized using these catalysts, it was decided to use Fe<sub>2</sub>Co/Al<sub>2</sub>O<sub>3</sub> catalysts for the synthesis of MWCNT@Al<sub>2</sub>O<sub>3</sub> composite supports. The choice was made because these catalysts have the highest activity in the MWCNT growth reaction at temperatures below 700 °C. The latter is crucial since at temperatures above 700 °C a phase transition from γ-Al<sub>2</sub>O<sub>3</sub> to δ-Al<sub>2</sub>O<sub>3</sub> begins. To optimize the structural characteristics and morphology of the MWCNT@Al<sub>2</sub>O<sub>3</sub> composite supports, the content of the Fe<sub>2</sub>Co active component was varied from 0.5 to 10 wt%. The content of supported metals in the catalyst samples was determined by XRF. According to the obtained results for all studied samples, Fe<sub>2</sub>Co content coincides with the calculated data. The phase composition of the obtained Fe<sub>2</sub>Co/Al<sub>2</sub>O<sub>3</sub> samples was studied by XRD (Fig. S1). X-ray diffraction data for

**Table 1**Characteristics of Al<sub>2</sub>O<sub>3</sub>, MWCNT, and MWCNT@Al<sub>2</sub>O<sub>3</sub> composite supports.

Sample	MWCNT yield <sup>*</sup> , gMWCNT/gFe <sub>2</sub> Co	S <sub>BET</sub> , m <sup>2</sup> /g	Pore volume, cm <sup>3</sup> /g	Moisture capacity, ml/g	C <sup>***</sup> , wt%
Al <sub>2</sub> O <sub>3</sub>	-	199	0.75	0.9	-
MWCNT(0.5% Fe <sub>2</sub> Co)@Al <sub>2</sub> O <sub>3</sub>	14.7	214	0.65	0.8	10.1
MWCNT(1% Fe <sub>2</sub> Co)@Al <sub>2</sub> O <sub>3</sub>	11.9	209	0.63	0.7	13.4
MWCNT(1.5% Fe <sub>2</sub> Co)@Al <sub>2</sub> O <sub>3</sub>	8.8	206	0.62	0.7	16.6
MWCNT(3% Fe <sub>2</sub> Co)@Al <sub>2</sub> O <sub>3</sub>	7.7	227	0.62	0.7	22.6
MWCNT(5% Fe <sub>2</sub> Co)@Al <sub>2</sub> O <sub>3</sub>	8.8	238	0.69	0.9	34.4
MWCNT(10% Fe <sub>2</sub> Co)@Al <sub>2</sub> O <sub>3</sub>	8.1	232	0.68	1.1	52.3
MWCNT <sup>***</sup>	11.6	275	1.08	2.8	n.d.

<sup>\*</sup> Activity of x%Fe<sub>2</sub>Co/Al<sub>2</sub>O<sub>3</sub> samples in the MWCNT growth reaction (C<sub>2</sub>H<sub>4</sub>:Ar = 1:1, flow rate of 400 ml/min, synthesis time 15 min, temperature of 680 °C). The yield of MWCNTs was calculated per mass of the Fe<sub>2</sub>Co active component. The MWCNTs yield averaged data obtained during three different experiments are presented.

<sup>\*\*</sup> Carbon content in MWCNT@Al<sub>2</sub>O<sub>3</sub> according to CHNS analysis.

<sup>\*\*\*</sup> MWCNTs were obtained by CVD of ethylene on a catalyst containing 40 wt% of Fe<sub>2</sub>Co as an active component and Al-containing oxides as support prepared by the Pechini method [39].

(0.5–5 wt%) Fe<sub>2</sub>Co/Al<sub>2</sub>O<sub>3</sub> samples showed the presence of highly defective and poorly crystallized Fe and Co oxide phases with a spinel structure and an average coherent scattering region size of less than 3 nm. However, in the case of 10 wt% Fe<sub>2</sub>Co/Al<sub>2</sub>O<sub>3</sub> sample, more intense reflections are observed, which are characteristic of cobalt oxide (Co<sub>3</sub>O<sub>4</sub>) with a spinel structure (cubic Fd-3m). The CSR size for this sample is 5 nm.

The activity of x% Fe<sub>2</sub>Co/Al<sub>2</sub>O<sub>3</sub> samples in the reaction of MWCNT growth, as well as textural characteristics, moisture capacity, and carbon content of MWCNT@Al<sub>2</sub>O<sub>3</sub> composite supports are presented in Table 1.

It can be seen from the obtained results that MWCNTs yield per mass of the active component decreases with an increase in the Fe<sub>2</sub>Co content in x%Fe<sub>2</sub>Co/Al<sub>2</sub>O<sub>3</sub> samples from 0.5 to 10 wt%. The maximum specific yield of MWCNTs (g MWCNTs/g Fe<sub>2</sub>Co) is observed for Fe<sub>2</sub>Co content of 0.5–1 wt%. A further decrease in the specific yield of MWCNTs with an

increase in Fe<sub>2</sub>Co content from 1.5 to 10 wt% is apparently associated with an increase in the particle size of the active component for MWCNTs growth. The specific surface area of MWCNT@Al<sub>2</sub>O<sub>3</sub> composite supports ranges from 206 to 238 m<sup>2</sup>g<sup>-1</sup> (Table 1). Pore volume and moisture capacity of MWCNT(0.5–3% Fe<sub>2</sub>Co)@Al<sub>2</sub>O<sub>3</sub> decrease compared to the initial Al<sub>2</sub>O<sub>3</sub> by 17.3% and 22.2%, respectively. Whereas, in the case of MWCNT(5–10% Fe<sub>2</sub>Co)@Al<sub>2</sub>O<sub>3</sub>, both pore volume, and moisture capacity increase, which is associated with the formation of secondary porosity due to the growth of extended MWCNT agglomerates on the surface of alumina particles.

Nitrogen adsorption-desorption isotherms, and the corresponding pore size distributions of Al<sub>2</sub>O<sub>3</sub>, MWCNT, and MWCNT@Al<sub>2</sub>O<sub>3</sub> composite supports, are shown in Fig. 1. In addition, cumulative pore volume curves of the studied supports are presented in Fig. S2. The shape of the obtained isotherms for all samples is close to type IVa, which is a characteristic of mesoporous materials [42]. The hysteresis loop due to

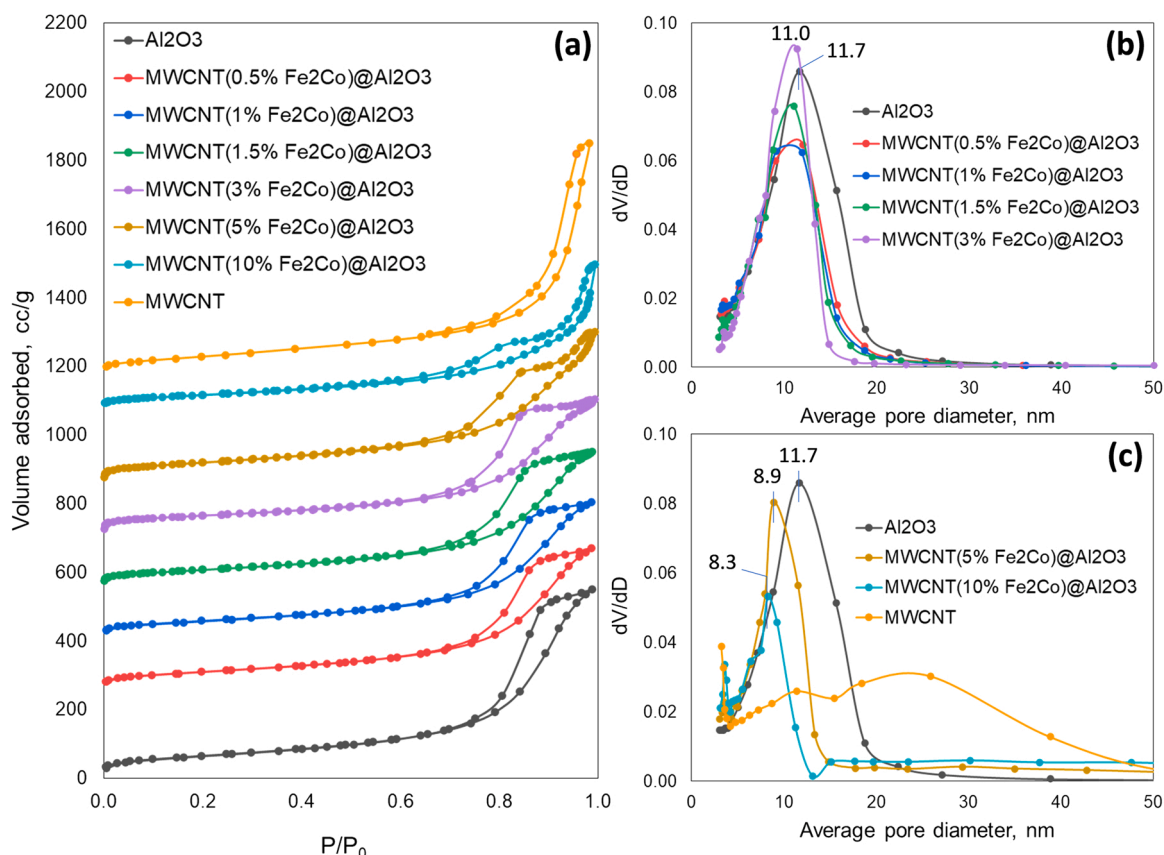


**Fig. 1.** Adsorption-desorption isotherms (a) and pore size distribution curves (b-c) of MWCNT@Al<sub>2</sub>O<sub>3</sub> composite supports, Al<sub>2</sub>O<sub>3</sub>, and MWCNT samples.



capillary condensation in mesopores is clearly visible in the range of relative pressures from 0.7 to 1.0. The shape of the hysteresis loop for the  $\text{Al}_2\text{O}_3$  sample is close to type H2(a). The adsorption and desorption branches of the isotherm are not parallel, and the desorption branch is steeper. However, since the saturation plateau is not well-defined, and the hysteresis loop is not closed until the relative pressure approaches 1, it can be considered that the hysteresis loop also has a feature of type H3. This isotherm shape is consistent with slit-shaped pores of  $\text{Al}_2\text{O}_3$  formed of aggregates of nanoparticles. The hysteresis loop for the MWCNT sample is the mixture of type H1 (without a well-defined saturation plateau at higher  $P/P_0$ ) and type H3 (without cavitation-induced evaporation step on the desorption branch). For MWCNT(0.5–3%  $\text{Fe}_2\text{Co}$ )@ $\text{Al}_2\text{O}_3$  composite supports, a slight decrease in the isotherm level is noted compared to the initial  $\text{Al}_2\text{O}_3$ . However, the shape of the hysteresis loop remains practically unchanged. An analysis of the pore size distribution curves shows that for MWCNT(0.5–3%  $\text{Fe}_2\text{Co}$ )@ $\text{Al}_2\text{O}_3$  a monomodal pore diameter distribution is observed in the range of 4–18 nm with a maximum at 11.0 nm (Fig. 1(b)). In this case, there is a slight decrease in the maximum average pore diameter from 11.7 to 11.0 nm compared to the initial alumina. Thus, treating 0.5–3%  $\text{Fe}_2\text{Co}/\text{Al}_2\text{O}_3$  catalysts in an ethylene flow at a temperature of 680 °C leads to a uniform growth of MWCNTs on the alumina surface. At the same time, the shape of the support pores is predominantly retained.

For MWCNT@ $\text{Al}_2\text{O}_3$  composite supports obtained from 5% to 10%  $\text{Fe}_2\text{Co}/\text{Al}_2\text{O}_3$  samples changes in nitrogen adsorption isotherms and pore size distribution curves are more pronounced (Fig. 1(a, c)). In this case, hysteresis loops comprise type H2(a) and type H3 and have an intermediate shape between loops observed for  $\text{Al}_2\text{O}_3$  and MWCNT samples. The contribution of the initial alumina mesopores decreases significantly, which is associated with an increase in both  $\text{Fe}_2\text{Co}$  and MWCNTs content. In the region of high relative pressures ( $P/P_0$  above 0.9), there is a sharp increase in the amount of adsorbed nitrogen without saturation of the adsorption isotherm (Fig. 1(a)). This indicates the appearance of macropores in MWCNT(5–10%  $\text{Fe}_2\text{Co}$ )@ $\text{Al}_2\text{O}_3$  supports, which are formed by MWCNTs interlacing during their growth under the action of intermolecular forces [13]. The presence of macropores in MWCNT(5–10%  $\text{Fe}_2\text{Co}$ )@ $\text{Al}_2\text{O}_3$  composite supports is also confirmed by a significant increase in moisture capacity (Table 1) without an increase in the nitrogen adsorption pore volume. In addition, the pore size distribution curves show the appearance of a peak with a maximum at about 4 nm, which corresponds to the diameter of the internal channels of MWCNTs (Fig. 1(c)). The pore size distribution of MWCNT(5–10%  $\text{Fe}_2\text{Co}$ )@ $\text{Al}_2\text{O}_3$  samples becomes narrower and shifts to 4–15 nm with a maximum at 8.9 and 8.3 nm, respectively. The difference between the average pore diameters of these samples (8.3 and 8.9 nm, respectively) and the average pore diameter of the  $\text{Al}_2\text{O}_3$  sample (11.7 nm) is 3.4 and 2.8 nm, which corresponds to the formation in their composition of MWCNTs containing ~ 8–10 walls (the thickness of one graphene layer in MWCNTs is 0.34 nm [43]).

According to the BJH method, in the case of a neat MWCNT sample, the pores formed by the interaction of isolated nanotubes have a wider diameter distribution (4–40 nm with a maximum at about 20–25 nm) as compared to composite support samples (Fig. 1(b-c)). The contribution of these pores to the total pore volume is much higher than the contribution of pores from the internal channels of MWCNTs with a maximum of ca. 4 nm.

The values on the contribution of the pores with different diameters for MWCNT@ $\text{Al}_2\text{O}_3$  composite supports calculated from nitrogen physisorption data are shown in Table 2. According to the obtained results, the mesopores with the diameters of 7–13 and 13–50 nm predominate in MWCNT(0.5–10%  $\text{Fe}_2\text{Co}$ )@ $\text{Al}_2\text{O}_3$  samples. With  $\text{Fe}_2\text{Co}$  content increase from 0.5 to 3 wt%, the proportion of the pores with a diameter of 7–13 nm increases by 31%. At the same time, the proportion of the pores with a diameter of 13–50 nm decreases by 44%. A further increase in  $\text{Fe}_2\text{Co}$  content from 5 to 10 wt% leads to a decrease in the proportion of 7–50 nm mesopores and the growth of larger pores (>

**Table 2**

Contribution of the pores with a different diameter in the pore volume of MWCNT@ $\text{Al}_2\text{O}_3$  composite supports,  $\text{Al}_2\text{O}_3$ , and MWCNT samples.

Sample	Pore size distribution (BJH), %			
	< 7 nm	7–13 nm	13–50 nm	> 50 nm
$\text{Al}_2\text{O}_3$	8	35	53	4
MWCNT(0.5% $\text{Fe}_2\text{Co}$ )@ $\text{Al}_2\text{O}_3$	12	42	43	3
MWCNT(1% $\text{Fe}_2\text{Co}$ )@ $\text{Al}_2\text{O}_3$	12	45	40	3
MWCNT(1.5% $\text{Fe}_2\text{Co}$ )@ $\text{Al}_2\text{O}_3$	11	57	29	3
MWCNT(3% $\text{Fe}_2\text{Co}$ )@ $\text{Al}_2\text{O}_3$	11	61	24	4
MWCNT(5% $\text{Fe}_2\text{Co}$ )@ $\text{Al}_2\text{O}_3$	12	57	19	12
MWCNT(10% $\text{Fe}_2\text{Co}$ )@ $\text{Al}_2\text{O}_3$	13	30	27	30
MWCNT	7	11	76	6

50 nm in diameter). Such changes are explained by a secondary porosity appearance due to the formation of agglomerates from intertwined MWCNTs. It should be noted that the proportion of small mesopores less than 7 nm in diameter for all composite supports does not exceed 11–13%.

X-ray diffraction data for MWCNT@ $\text{Al}_2\text{O}_3$  composite supports as well as data for the initial MWCNT and alumina as reference samples are presented in Fig. 2. It can be seen that the reflections characteristic of MWCNTs appear in the range of  $2\theta$  angles ~ 25.5 ° only for MWCNT@ $\text{Al}_2\text{O}_3$  composite supports obtained from 5% to 10%  $\text{Fe}_2\text{Co}/\text{Al}_2\text{O}_3$  samples. In this case, the CSR size along the [002] direction for MWCNTs in MWCNT(5–10%  $\text{Fe}_2\text{Co}$ )@ $\text{Al}_2\text{O}_3$  composite supports is 3 nm, which corresponds to the thickness of MWCNTs consisting of about 9 walls (the thickness of one graphene layer in MWCNTs is 0.34 nm [43]). This is in good agreement with the obtained results on the difference between the average pore diameters of composite supports and the  $\text{Al}_2\text{O}_3$  sample (Fig. 1(c)).

The phase composition of the initial alumina is represented by the  $\gamma$ - $\text{Al}_2\text{O}_3$  phase, and it does not change during the synthesis of composite supports under the conditions of the MWCNT growth reaction [25,44].

In the case of the MWCNT(10%  $\text{Fe}_2\text{Co}$ )@ $\text{Al}_2\text{O}_3$  sample, the reflections corresponding to FeCo alloy with a CSR size of 6 nm are observed. Metallic Co is not present, which is evident by the absence of a reflection at 52°. This indicates that under the conditions of the MWCNTs synthesis reaction, the active FeCo alloy is formed [38].

For a detailed assessment of the degree of structural ordering and defectiveness of MWCNTs formed in MWCNT(0.5–10%  $\text{Fe}_2\text{Co}$ )@ $\text{Al}_2\text{O}_3$

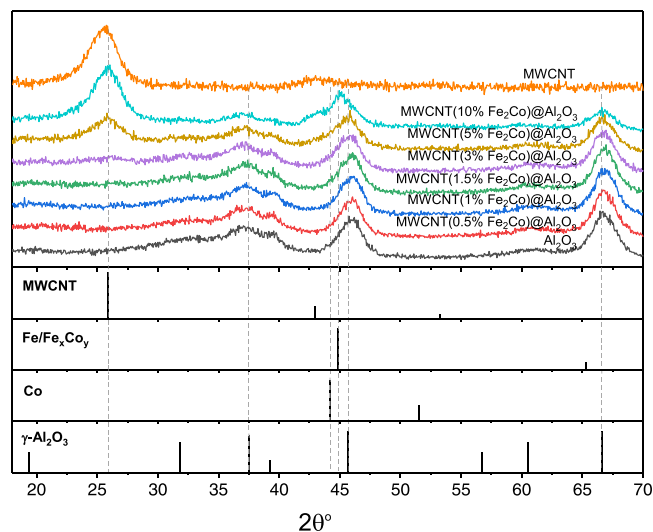


**Fig. 2.** X-ray patterns of MWCNT@ $\text{Al}_2\text{O}_3$  composite supports,  $\text{Al}_2\text{O}_3$ , and MWCNT samples. Major peaks of  $\text{Fe}_x\text{Co}_y$  and Fe phases are similar and shown in one plot.

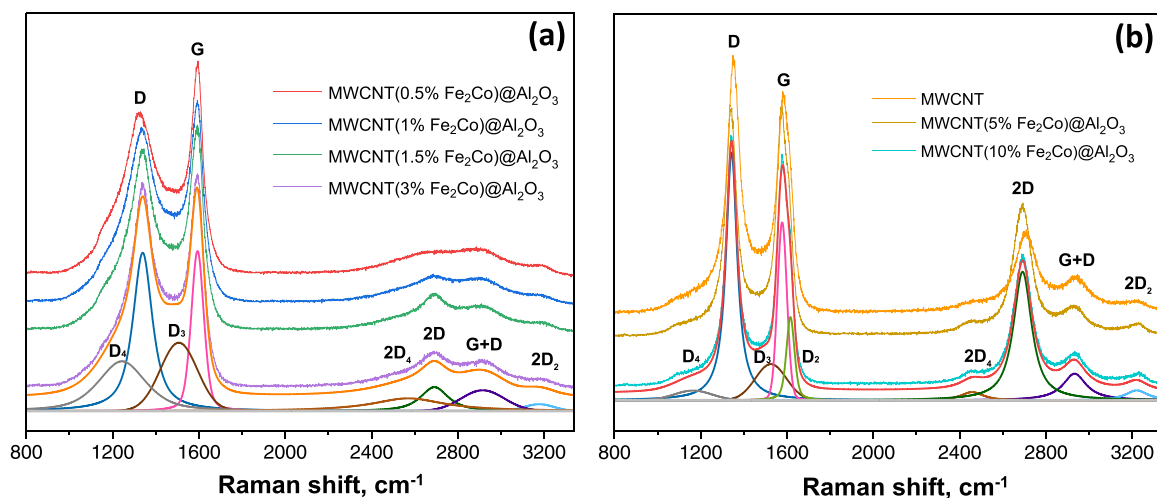


**Fig. 3.** Raman spectra of MWCNT(0.5–3% Fe<sub>2</sub>Co)/Al<sub>2</sub>O<sub>3</sub> (a) and MWCNT(5–10% Fe<sub>2</sub>Co)/Al<sub>2</sub>O<sub>3</sub> (b) composite supports. Examples of the decomposition of Raman spectra are presented for MWCNT(3% Fe<sub>2</sub>Co)/Al<sub>2</sub>O<sub>3</sub> (a) and MWCNT(10% Fe<sub>2</sub>Co)/Al<sub>2</sub>O<sub>3</sub> (b) samples.

composite supports, Raman spectroscopy was used. The Raman spectra of all samples were deconvoluted by pseudo-Voigt functions using the Fityk program (Fig. 3(a–b)). It is known that the analysis of the position and intensity of the bands in the Raman spectra of various carbon materials makes it possible to identify not only the type of carbon material but also fix even subtle differences in its structure.

Raman spectra of MWCNT(0.5–10% Fe<sub>2</sub>Co)/Al<sub>2</sub>O<sub>3</sub> composite supports can be deconvoluted into nine components in the 800–3400 cm<sup>−1</sup> range [45]. Among the main first-order bands present in spectra, one can note the D (~1340 cm<sup>−1</sup>) and G (~1590 cm<sup>−1</sup>) bands, which correspond to the graphite lattice vibration modes with A<sub>1</sub>g symmetry and the ideal graphite lattice mode with E<sub>2</sub>g symmetry, respectively. The remaining first-order bands D<sub>2</sub>, D<sub>3</sub>, and D<sub>4</sub> present in Raman spectra of composite supports characterize the structural disorder of the carbon material in their composition. The D<sub>2</sub> band at ~1615 cm<sup>−1</sup> characterizes the presence of surface graphene layers with E<sub>2</sub>g-symmetry. The D<sub>3</sub> band (~1500 cm<sup>−1</sup>) corresponds to the amorphous fraction of carbon originating from organic molecules, fragments, or functional groups. The D<sub>4</sub> band (~1190 cm<sup>−1</sup>) corresponds to the disordering of the graphite lattice with A<sub>1</sub>g symmetry, as well as to the stretching vibrations of C–C and C=C bonds in polyene-like structures.

In addition, Raman spectra of composite supports exhibit second-order 2D<sub>4</sub>, 2D, G+D, and 2D<sub>2</sub> bands located approximately at 2450, 2700, 2940, and 3215 cm<sup>−1</sup>, which can be attributed to overtones and combinations of known lattice vibration modes. The presence of the 2D<sub>4</sub>, G+D, and 2D<sub>2</sub> bands in the Raman spectra of MWCNT@Al<sub>2</sub>O<sub>3</sub> also indicates that the carbon material is disordered. Analysis of the 2D band behavior is mainly used to characterize the number of graphene layers and their mutual orientation (stacking order). Intense 2D bands are observed only for samples with extended graphene fragments. Graphene fragments of small size mainly belong to polyaromatic molecules, for which 2D bands are uncharacteristic [46]. Estimation of the integrated intensities ratio of the D/G, 2D/G, D<sub>3</sub>/G, D<sub>4</sub>/G, and D<sub>2</sub>/G bands provides unique information about the structure and defectiveness type of MWCNT in MWCNT@Al<sub>2</sub>O<sub>3</sub> samples (Fig. 4). According to the obtained results, Fe<sub>2</sub>Co content growth from 0.5 to 10 wt% leads to a gradual increase in the ID/IG ratio from 1.6 to 2.4 for MWCNT@Al<sub>2</sub>O<sub>3</sub> composite supports. This behavior is associated with an increase in the samples structural disorder caused by a change in the material mesoporosity (an increase in the fraction of smaller mesopores (~9 nm)) (Fig. 1(c)).

It should be noted that the I<sub>2D</sub>/I<sub>G</sub> bands integrated intensities ratio slightly increases for MWCNT(0.5–3% Fe<sub>2</sub>Co)/Al<sub>2</sub>O<sub>3</sub> composite supports and sharply increases for MWCNT(5–10% Fe<sub>2</sub>Co)/Al<sub>2</sub>O<sub>3</sub> samples

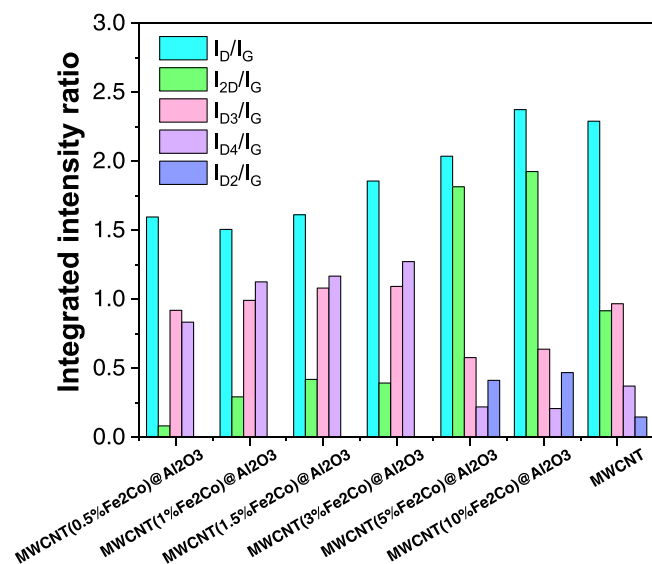


**Fig. 4.** The integrated intensities ratio of the D, 2D, D<sub>3</sub>, D<sub>4</sub>, and D<sub>2</sub>/G bands, calculated based on the deconvolution of Raman spectra of MWCNT(0.5–10% Fe<sub>2</sub>Co)/Al<sub>2</sub>O<sub>3</sub> composite supports as a function of Fe<sub>2</sub>Co content used for MWCNT synthesis.

from 0.4 to 1.9, which is associated with an increase in the size of MWCNTs graphene fragment. Interestingly, for the neat MWCNT sample, the I<sub>2D</sub>/I<sub>G</sub> ratio is two times lower. This indicates that MWCNTs in MWCNT(5% and 10% Fe<sub>2</sub>Co)/Al<sub>2</sub>O<sub>3</sub> composite supports have a larger graphene fragment. The I<sub>D3</sub>/I<sub>G</sub> and I<sub>D4</sub>/I<sub>G</sub> ratios, which are responsible for the content of amorphous carbon and disorder of the graphite lattice caused by vibrations from single- and double-bonded carbon of polyene structures [47] and ionic impurities [48], demonstrate only slight changes for MWCNTs in MWCNT(0.5–3% Fe<sub>2</sub>Co)/Al<sub>2</sub>O<sub>3</sub> composite supports. In contrast, a significant decrease in the integral intensities of these bands is observed for MWCNT(5–10% Fe<sub>2</sub>Co)/Al<sub>2</sub>O<sub>3</sub>, which indicates a decrease in the defectiveness of MWCNTs in their composition. It should be noted that the contribution from the D<sub>2</sub> band responsible for stacking faults in graphene layers could only be distinguished for MWCNT(5–10% Fe<sub>2</sub>Co)/Al<sub>2</sub>O<sub>3</sub> composite supports and neat MWCNT. At the same time, for neat MWCNT, the value of I<sub>D2</sub>/I<sub>G</sub> is lower than for MWCNT(5–10% Fe<sub>2</sub>Co)/Al<sub>2</sub>O<sub>3</sub> samples, for which this ratio of integrated band intensities is similar. Thus, MWCNTs in MWCNT(0.5–3% Fe<sub>2</sub>Co)/Al<sub>2</sub>O<sub>3</sub> composite supports are characterized by a



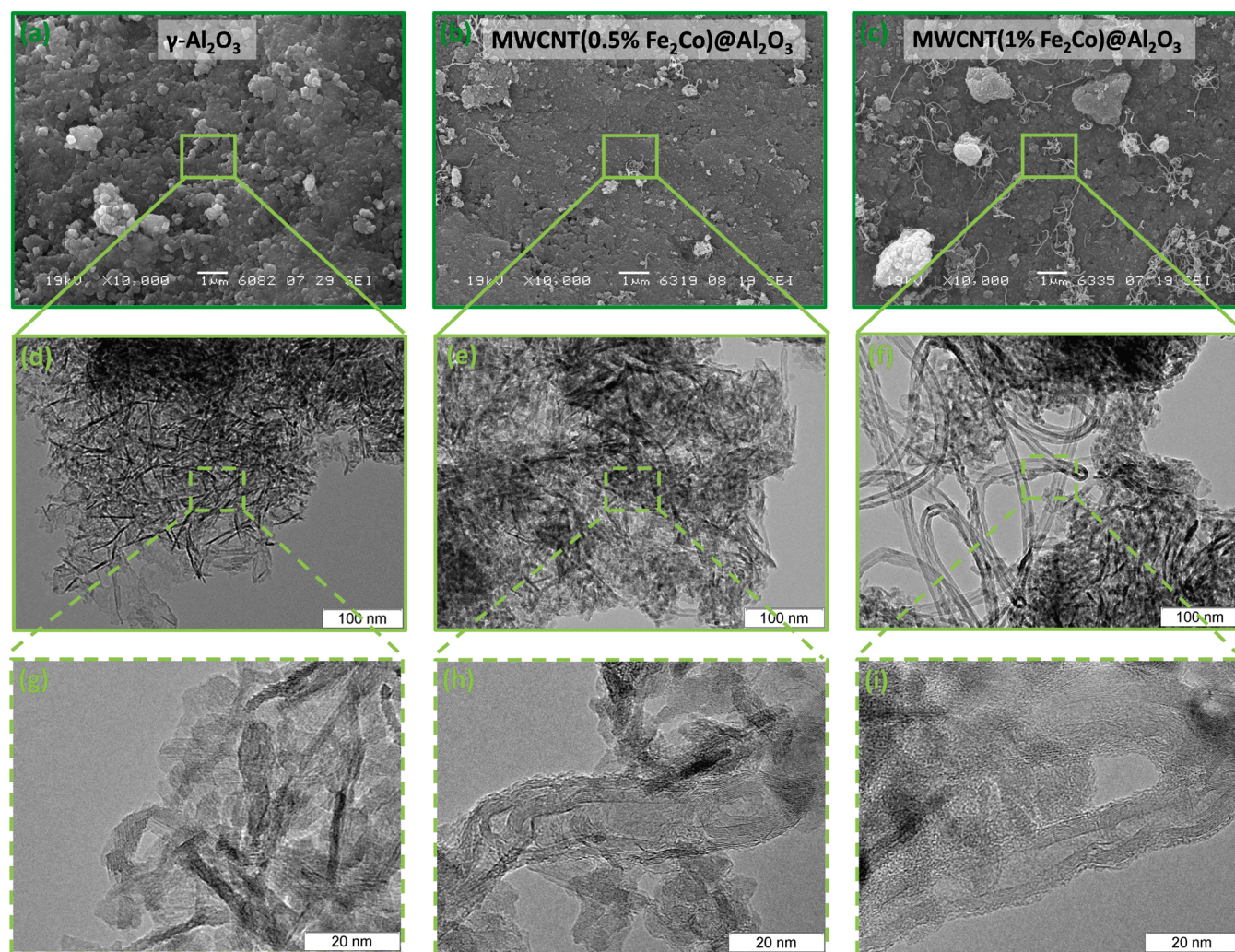


Fig. 5. Typical SEM (a-c) and TEM (d-i) images of  $\gamma$ - $\text{Al}_2\text{O}_3$ , MWCNT(0.5%  $\text{Fe}_2\text{Co}$ )@ $\text{Al}_2\text{O}_3$ , and MWCNT(1%  $\text{Fe}_2\text{Co}$ )@ $\text{Al}_2\text{O}_3$  composite supports.

higher degree of structural defectiveness and a shorter graphene fragment length compared to MWCNT(5–10%  $\text{Fe}_2\text{Co}$ )@ $\text{Al}_2\text{O}_3$  and neat MWCNT samples.

The morphology and structural characteristics of MWCNT(0.5–10%  $\text{Fe}_2\text{Co}$ )@ $\text{Al}_2\text{O}_3$  composite supports were studied by SEM and TEM (Figs. 5–7). The initial alumina sample is represented by a mixture of polycrystalline lamellar particles with a size of up to 5 nm and needle-shaped particles with a length of more than 20 nm.

SEM and TEM data show that MWCNT(0.5–1%  $\text{Fe}_2\text{Co}$ )@ $\text{Al}_2\text{O}_3$  samples are represented by a mixture of polycrystalline lamellar and needle-shaped particles of initial  $\text{Al}_2\text{O}_3$  entwined with single MWCNTs (Fig. 5). At the same time, with an increase in  $\text{Fe}_2\text{Co}$  content, the number of individual MWCNTs intertwining alumina crystallites increases. It should be noted that MWCNTs in MWCNT(0.5–1%  $\text{Fe}_2\text{Co}$ )@ $\text{Al}_2\text{O}_3$  composite supports are characterized by high defectiveness, which is in good agreement with the Raman spectroscopy data (Figs. 3(a) and 4). High-resolution TEM images show that the nanotube fragments in the region of the bends have smooth, rounded contours. Meanwhile, on the surface of the nanotubes, a large number of fullerene-like formations and short misoriented graphite fragments are observed. Graphene-like layers of nanotubes are characterized by the presence of many defects (discontinuities, layer mismatches, Y-like connections, etc.). In some areas, there is a discrepancy in the number of layers on different sides of MWCNTs. The latter indicates the presence of open extended graphene layers, mainly localized inside the tubes. At the same time, it is not possible to conduct a statistical study of the structural characteristics of

MWCNTs in the composition of MWCNT(0.5–1%  $\text{Fe}_2\text{Co}$ )@ $\text{Al}_2\text{O}_3$  supports due to their low content.

An increase in  $\text{Fe}_2\text{Co}$  content from 1.5 to 10 wt% leads to the more intensive growth of MWCNTs in MWCNT(1.5–10%  $\text{Fe}_2\text{Co}$ )@ $\text{Al}_2\text{O}_3$  composite supports. According to SEM data, the morphology of MWCNT (1.5–3%  $\text{Fe}_2\text{Co}$ )@ $\text{Al}_2\text{O}_3$  samples is mainly represented by coils of intertwined individual nanotubes with inclusions of a mixture of initial  $\gamma$ - $\text{Al}_2\text{O}_3$  particles (Fig. 6(a–b)). In the case of MWCNT(5%  $\text{Fe}_2\text{Co}$ )@ $\text{Al}_2\text{O}_3$  composite support, the formation of strands of intertwined MWCNTs covering the surface of alumina crystallites is observed (Fig. 6(c)). A further increase in  $\text{Fe}_2\text{Co}$  content up to 10 wt% leads to the growth of arrays of vertically oriented MWCNTs in MWCNT(10%  $\text{Fe}_2\text{Co}$ )@ $\text{Al}_2\text{O}_3$ .

Statistical analysis of TEM images shows that an increase in  $\text{Fe}_2\text{Co}$  content leads to the growth of MWCNTs with different structural characteristics (Fig. 7(a–d)) in the composition of MWCNT(1.5–10%  $\text{Fe}_2\text{Co}$ )@ $\text{Al}_2\text{O}_3$  supports. Thus, MWCNTs average outer and inner diameters increase from 7.4 to 10 nm and 3.1–4.3 nm with an increase in  $\text{Fe}_2\text{Co}$  content from 1.5 to 10 wt%, respectively. It should be noted that MWCNTs grown on 5 and 10 wt%  $\text{Fe}_2\text{Co}/\text{Al}_2\text{O}_3$  samples are characterized by lower defects, which is in agreement with the Raman spectroscopy data (Figs. 3(b) and 4).

### 3.2. Characterization of CoMoS/MWCNT@ $\text{Al}_2\text{O}_3$ catalysts

Comparison of textural characteristics of MWCNT@ $\text{Al}_2\text{O}_3$  composite supports and CoMoS/MWCNT@ $\text{Al}_2\text{O}_3$  catalysts shows that the shape of

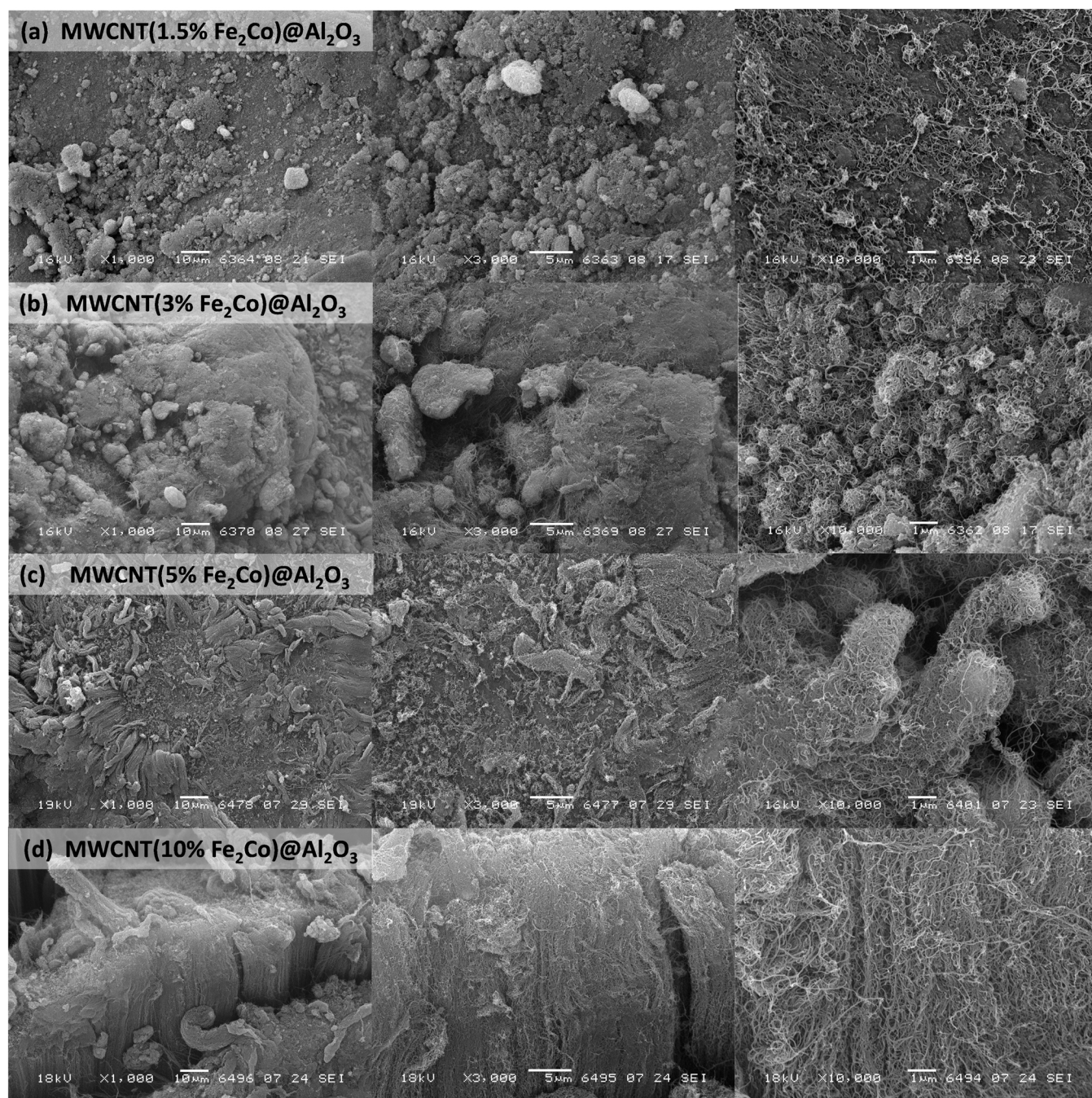
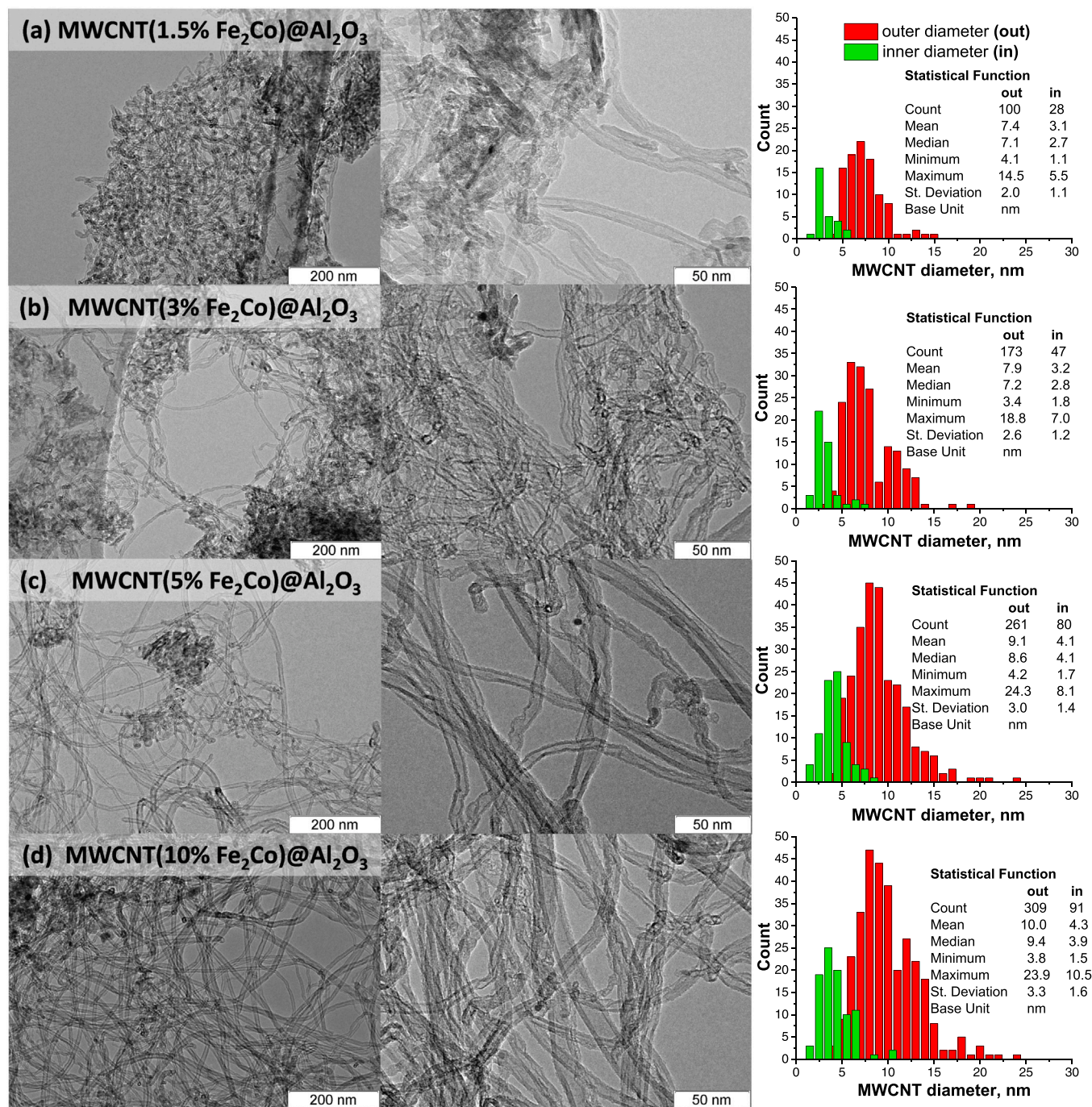


Fig. 6. SEM images of MWCNT(1.5–10% Fe<sub>2</sub>Co)@Al<sub>2</sub>O<sub>3</sub> composite supports.





**Fig. 7.** TEM images of MWCNT(1.5–10% Fe<sub>2</sub>Co)@Al<sub>2</sub>O<sub>3</sub> composite supports and distribution histograms of outer (out) and inner (in) diameters of MWCNTs in their composition.

adsorption-desorption isotherms and the type of hysteresis loop do not change significantly after the supporting of active metals and sulfidation (Fig. 8). At the same time, the amount of adsorbed nitrogen decreases significantly. In addition, for CoMoS/MWCNT@Al<sub>2</sub>O<sub>3</sub> catalysts, hysteresis loop broadening in the range from 0.5 to 1.0 is observed compared to the initial supports (Figs. 1 and 8). However, the pore size distribution is retained (Figs. 1, 8, and S2-S3). It should be noted that a decrease in the height of the pore size distribution curve occurs for all CoMoS/MWCNT@Al<sub>2</sub>O<sub>3</sub> catalysts and in the entire range of pores. Thus, it can be assumed that the distribution of the sulfide component in the pores of MWCNT@Al<sub>2</sub>O<sub>3</sub> composite supports is uniform.

The supporting of active metals leads to a decrease in the specific surface area and pore volume of CoMoS catalysts compared to the initial

supports (Table 1 and Table 3), as well as to a redistribution of mesopore diameters in the range of < 7–50 nm. According to the obtained results, there is a decrease in the proportion of pores with a diameter of 7–13 nm and an increase in the proportion of pores with a diameter of < 7 nm. However, it should be noted that mesopores with diameters of 7–13 and 13–50 nm still dominate in CoMoS/MWCNT@Al<sub>2</sub>O<sub>3</sub> catalysts pore size distribution. The significant decrease in surface area and pore volume of the catalysts compared to the initial supports is due to the high CoMo loading.

To evaluate the changes in the morphology of the active sulfide component depending on the type of support, sulfided CoMo catalysts were studied by high-resolution TEM (Fig. 9, S4-S5). The active component of the CoMo hydrotreating catalyst is molybdenum disulfide

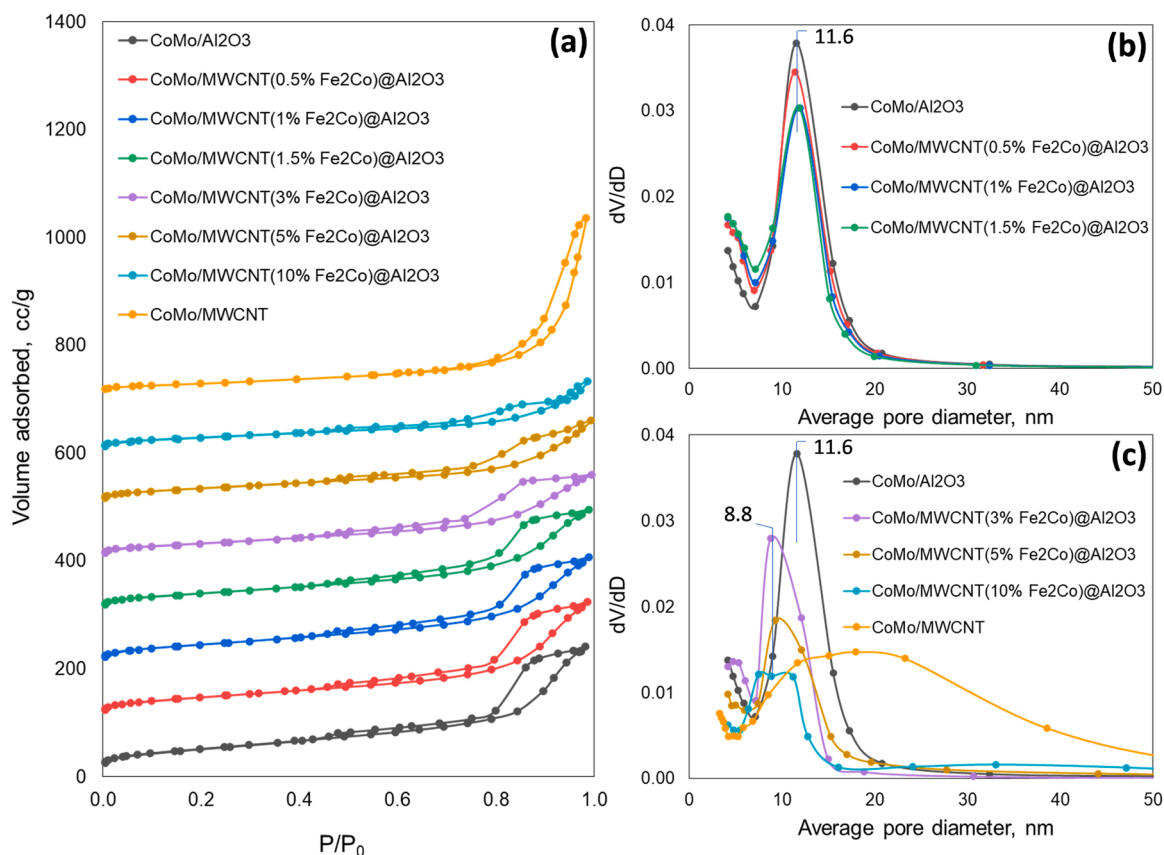


Fig. 8. Adsorption-desorption isotherms (a) and pore size distribution curves (b-c) of CoMoS/MWCNT@Al<sub>2</sub>O<sub>3</sub>, CoMoS/Al<sub>2</sub>O<sub>3</sub>, and CoMoS/MWCNT catalysts.

Table 3

Textural characteristics of CoMoS/MWCNT@Al<sub>2</sub>O<sub>3</sub>, CoMoS/Al<sub>2</sub>O<sub>3</sub>, and CoMoS/MWCNT catalysts.

Sample	Surface area, m <sup>2</sup> /g	Pore volume, cm <sup>3</sup> /g	Pore size distribution (BJH), %			
			< 7 nm	7–13 nm	13–50 nm	> 50 nm
CoMoS/Al <sub>2</sub> O <sub>3</sub>	129	0.42	9	26	59	6
CoMoS/MWCNT(0.5% Fe <sub>2</sub> Co)/Al <sub>2</sub> O <sub>3</sub>	170	0.35	22	31	42	5
CoMoS/MWCNT(1% Fe <sub>2</sub> Co)/Al <sub>2</sub> O <sub>3</sub>	159	0.32	24	30	41	5
CoMoS/MWCNT(1.5% Fe <sub>2</sub> Co)/Al <sub>2</sub> O <sub>3</sub>	142	0.30	24	34	38	4
CoMoS/MWCNT(3% Fe <sub>2</sub> Co)/Al <sub>2</sub> O <sub>3</sub>	116	0.25	26	48	23	3
CoMoS/MWCNT(5% Fe <sub>2</sub> Co)/Al <sub>2</sub> O <sub>3</sub>	124	0.25	23	33	33	11
CoMoS/MWCNT(10% Fe <sub>2</sub> Co)/Al <sub>2</sub> O <sub>3</sub>	104	0.21	23	33	27	17
CoMoS/MWCNT	103	0.52	3	11	71	15

promoted with cobalt atoms, which form the so-called CoMoS phase. Analysis of TEM images demonstrates the presence of nano-sized layered particles of MoS<sub>2</sub>. According to TEM data, CoMoS/Al<sub>2</sub>O<sub>3</sub> catalyst is characterized by the highest value of the average slab length of MoS<sub>2</sub>, which is 3.3 nm (Fig. S4), while the average stacking number is 2.1 (Fig. S6 and Table 4). The sulfide component of the CoMoS/MWCNT catalyst is mainly represented by mono- and two-layer slabs with an average stacking number of 1.7 and an average slab length of 2.9 nm. It should be noted that in CoMoS/MWCNT catalyst, the sulfide particles are located both in the internal channels of MWCNTs and on their outer surface. There is no blocking of the internal channels since the sulfide particles are monolayer.

According to TEM data, CoMoS/MWCNT(0.5–10% Fe<sub>2</sub>Co)/Al<sub>2</sub>O<sub>3</sub> catalysts are characterized by the presence of sulfide particles both on the Al<sub>2</sub>O<sub>3</sub> surface and on MWCNT (surface and internal channels) (Fig. 9). The slab length varies from 0.8 to 11.5 nm with a predominance of particles with a length of 2–5 nm (Fig. 9). The average slab length depends on the support type and decreases from 3.2 to 2.6 nm when moving from CoMoS/MWCNT(0.5% Fe<sub>2</sub>Co)/Al<sub>2</sub>O<sub>3</sub> to CoMoS/MWCNT

(1.5% Fe<sub>2</sub>Co)/Al<sub>2</sub>O<sub>3</sub> catalyst. A further increase in the content of Fe<sub>2</sub>Co and, accordingly, the content of MWCNTs in composite support leads to a subsequent increase in the average slab length up to 3.1 nm for CoMoS/MWCNT(10% Fe<sub>2</sub>Co)/Al<sub>2</sub>O<sub>3</sub> catalyst (Table 4).

It should be noted that in CoMoS/MWCNT(0.5–10% Fe<sub>2</sub>Co)/Al<sub>2</sub>O<sub>3</sub> catalysts, mono-, two-, and three-layer sulfide slabs predominate. The ratio between them depends on the type of composite support used (Fig. S7). In addition, for CoMoS/MWCNT(5–10% Fe<sub>2</sub>Co)/Al<sub>2</sub>O<sub>3</sub> catalysts, sulfide particles with a stacking number of 6–8 are observed (Fig. S7 b).

As reported in [49], the activity of CoMoS catalysts directly depends on the ratio of edge-to-corner molybdenum atoms in MoS<sub>2</sub>, which is determined by the dispersion of sulfide particles. According to the obtained results, the dispersion of MoS<sub>2</sub> increases from 0.36 to 0.53–0.55 when moving from CoMoS/Al<sub>2</sub>O<sub>3</sub> to CoMoS/MWCNT(1.5–3% Fe<sub>2</sub>Co)/Al<sub>2</sub>O<sub>3</sub> catalysts (Table 4). A further increase in the content of MWCNTs in CoMoS/MWCNT(5–10% Fe<sub>2</sub>Co)/Al<sub>2</sub>O<sub>3</sub> catalysts leads to a decrease in MoS<sub>2</sub> dispersion to 0.45. Thus, the highest dispersion of sulfide particles is characteristic of CoMoS/MWCNT(1.5% Fe<sub>2</sub>Co)/Al<sub>2</sub>O<sub>3</sub> and



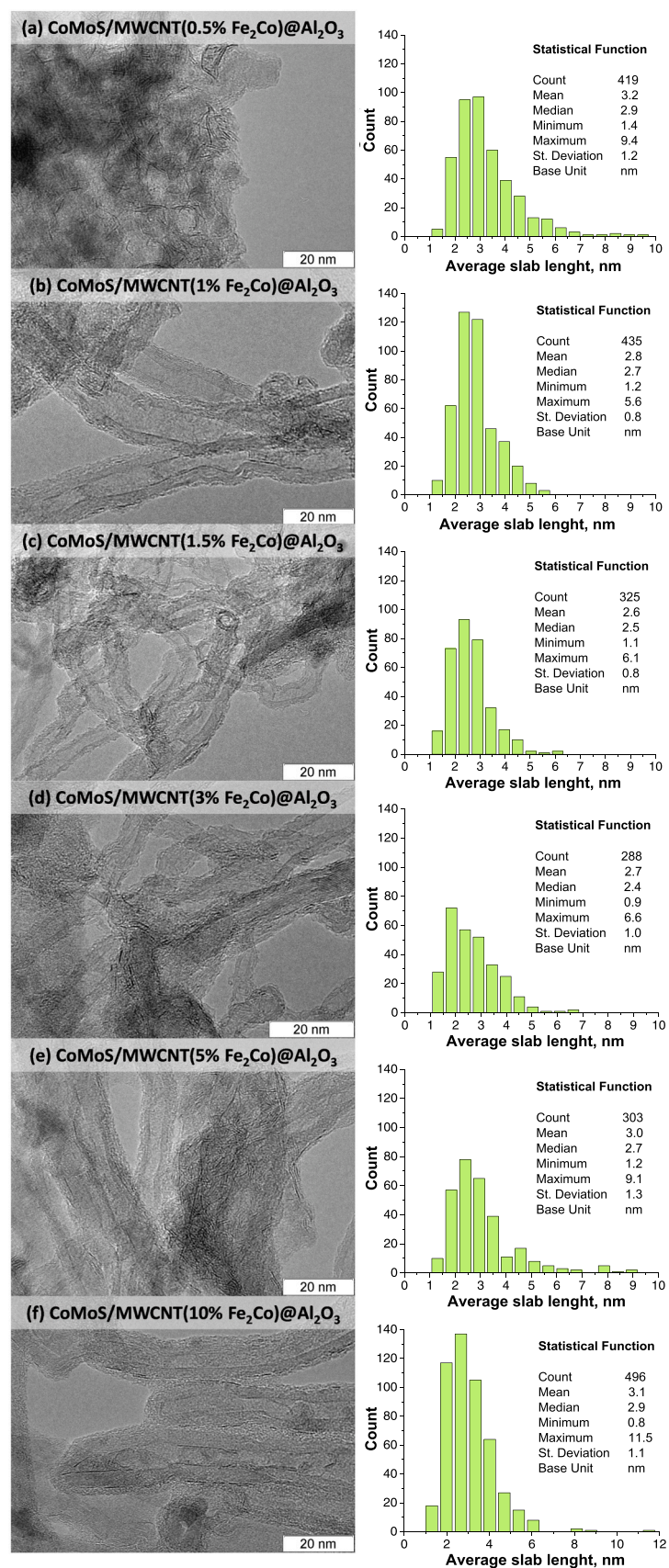


Fig. 9. TEM images of CoMoS/MWCNT(0.5–10% Fe<sub>2</sub>Co)@Al<sub>2</sub>O<sub>3</sub> catalysts (a-f) and distribution of sulfide particles slab length.

**Table 4**HRTEM data for CoMoS/MWCNT@Al<sub>2</sub>O<sub>3</sub>, CoMoS/Al<sub>2</sub>O<sub>3</sub>, and CoMoS/MWCNT catalysts.

Sample	Average stacking number	Average slab length, nm	Dispersion of MoS <sub>2</sub>	Mo <sub>e</sub> /Mo <sub>c</sub> ratio*
CoMoS/Al <sub>2</sub> O <sub>3</sub>	2.1	3.3	0.36	3.7
CoMoS/MWCNT(0.5% Fe <sub>2</sub> Co)@Al <sub>2</sub> O <sub>3</sub>	2.1	3.2	0.36	3.5
CoMoS/MWCNT(1% Fe <sub>2</sub> Co)@Al <sub>2</sub> O <sub>3</sub>	1.6	2.8	0.40	2.9
CoMoS/MWCNT(1.5% Fe <sub>2</sub> Co)@Al <sub>2</sub> O <sub>3</sub>	1.7	2.6	0.55	2.6
CoMoS/MWCNT(3% Fe <sub>2</sub> Co)@Al <sub>2</sub> O <sub>3</sub>	1.3	2.7	0.53	2.7
CoMoS/MWCNT(5% Fe <sub>2</sub> Co)@Al <sub>2</sub> O <sub>3</sub>	1.9	3.0	0.47	3.2
CoMoS/MWCNT(10% Fe <sub>2</sub> Co)@Al <sub>2</sub> O <sub>3</sub>	1.8	3.1	0.45	3.3
CoMoS/MWCNT	1.7	2.9	0.49	3.0

\* Edge-to-corner Mo atoms ratio in MoS<sub>2</sub>

CoMoS/MWCNT(3% Fe<sub>2</sub>Co)@Al<sub>2</sub>O<sub>3</sub> catalysts. In addition, these samples are characterized by lower average stacking number, which is 1.7 and 1.3, respectively (Table 4). As it was shown by Raman spectroscopy, MWCNTs in MWCNT(0.5–3% Fe<sub>2</sub>Co)@Al<sub>2</sub>O<sub>3</sub> composite supports are characterized by a higher degree of structural defectiveness and a shorter graphene fragment length as compared to MWCNT(5–10% Fe<sub>2</sub>Co)@Al<sub>2</sub>O<sub>3</sub> supports and neat MWCNT sample. Thus, the presence of a large number of structural defects in the MWCNTs walls ensures the formation of sulfide particles with higher dispersion (Table 4).

The surface elemental composition of MWCNT(0.5–10% Fe<sub>2</sub>Co)@Al<sub>2</sub>O<sub>3</sub> composite supports and the active phase of CoMoS/MWCNT(0.5–10% Fe<sub>2</sub>Co)@Al<sub>2</sub>O<sub>3</sub> catalysts was characterized by XPS. Al2p, O1s, C1s, Fe2p, and Co2p spectra of MWCNT(3% Fe<sub>2</sub>Co)@Al<sub>2</sub>O<sub>3</sub> sample are shown in Fig. S8. These spectra are typical for all studied MWCNT@Al<sub>2</sub>O<sub>3</sub> composite supports. An analysis of XPS spectra of MWCNT@Al<sub>2</sub>O<sub>3</sub> samples allows us to conclude that the surface composition of the supports does not contain Fe and Co elements.

XPS spectra, as well as the main results of Mo3d, Co2p, Al2p, and C1s spectra decomposition for CoMoS/MWCNT(1–10% Fe<sub>2</sub>Co)@Al<sub>2</sub>O<sub>3</sub> catalysts are shown in Fig. 10 and Table 5. Mo3d spectra (Fig. 10) of CoMoS/MWCNT(1–10% Fe<sub>2</sub>Co)@Al<sub>2</sub>O<sub>3</sub> catalysts are characterized by three main contributions corresponding to Mo<sup>4+</sup>, Mo<sup>5+</sup> and Mo<sup>6+</sup>. The binding energy of 229.0 ± 0.1 eV of the main peak for Mo3d spectra is similar for all catalysts and refers to Mo<sup>4+</sup> in MoS<sub>2</sub> [50]. Peaks with a binding energy of 230.5 ± 0.1 eV and 232.7 ± 0.1 eV correspond to molybdenum in 5 + and 6 + valence states, respectively. These valence states refer to MoS<sub>x</sub>O<sub>y</sub> and MoO<sub>3</sub> species [51]. It should be noted that for CoMoS/MWCNT(3% Fe<sub>2</sub>Co)@Al<sub>2</sub>O<sub>3</sub> catalyst, molybdenum in 6 + valence state is not observed. According to the decomposition of Mo3d spectra, the main state of molybdenum on the surface of all catalysts is Mo<sup>4+</sup> (69.7–79.4%).

The binding energy of the main Co2p peak for CoMoS/MWCNT(1–10% Fe<sub>2</sub>Co)@Al<sub>2</sub>O<sub>3</sub> catalysts is 779.1 ± 0.1 eV and is typical for cobalt in the CoMoS phase [51] (Fig. 10). The decomposition of Co2p spectra shows that the largest fraction of the CoMoS phase (71.3%) is observed for CoMoS/MWCNT(3% Fe<sub>2</sub>Co)@Al<sub>2</sub>O<sub>3</sub> catalyst. According to TEM data, this sample is also characterized by a higher dispersion of MoS<sub>2</sub> (Table 4). The binding energy of the main S2s peak in all samples is 226.6 ± 0.1 eV and belongs to the terminal S<sub>2</sub><sup>2-</sup>.

Fig. S9 compares typical C1s spectra of CoMoS/Al<sub>2</sub>O<sub>3</sub>, CoMoS/MWCNT, and CoMoS/MWCNT(3% Fe<sub>2</sub>Co)@Al<sub>2</sub>O<sub>3</sub> catalysts. C1s spectra of CoMoS/MWCNT(1–10% Fe<sub>2</sub>Co)@Al<sub>2</sub>O<sub>3</sub> catalysts are similar. Therefore, only the spectrum of CoMoS/MWCNT(3% Fe<sub>2</sub>Co)@Al<sub>2</sub>O<sub>3</sub> catalyst is presented in Fig. S9, for example. The results of the decomposition of C1s spectra for all catalysts are presented in Table S1. The energy of the main peak for CoMoS/MWCNT and CoMoS/MWCNT(1–10% Fe<sub>2</sub>Co)@Al<sub>2</sub>O<sub>3</sub> catalysts is 284.5 eV and corresponds to carbon with the graphite structure (sp<sup>2</sup> hybridization, C=C) arranged in hexagon walls of MWCNT [43]. Peaks located at 285.8 ± 0.1, 287.5 ± 0.1, and 289.4

± 0.1 eV correspond to hydroxyl (ether) (C-OH, C-O-C), carbonyl (C=O) and carboxyl (ester) groups (COOH, O-C=O), respectively [43]. The shake-up satellite peak at 291 eV corresponds to the π-π\* transition of carbon in aromatic rings. This feature is associated with the interaction of emitted photoelectrons with π electrons of the graphene structure [52]. The C/Al ratio increases with increasing MWCNTs content in CoMoS/MWCNT(1–10% Fe<sub>2</sub>Co)@Al<sub>2</sub>O<sub>3</sub> catalysts (Tables 1 and 5). This is associated with an increase in the total carbon content. As it follows from C1s spectra decomposition, with an increase in the MWCNTs content in MWCNT(1–10% Fe<sub>2</sub>Co)@Al<sub>2</sub>O<sub>3</sub> supports the sp<sup>2</sup> carbon decreases from 68.9% to 65.1%, which is compensated by a small increase in the content of all oxygen-containing functional groups (Table S1). It is interesting to note that carbon nanotubes in composite supports are in the oxidized state. The positions of the peaks corresponding to oxygen-containing functional groups in C1s spectra are similar for carbon nanotubes in the composition of MWCNT@Al<sub>2</sub>O<sub>3</sub> supports and MWCNT sample preliminarily oxidized in nitric acid. Apparently, the oxidation of carbon nanotubes in MWCNT@Al<sub>2</sub>O<sub>3</sub> occurs upon contact of the composite support with air during its unloading from the reactor immediately after synthesis. The C1s spectrum of the CoMoS/Al<sub>2</sub>O<sub>3</sub> sample is difficult to correctly decompose into individual components due to its low intensity. However, it can be seen that for this catalyst, the binding energy of the main C1s peak is 285.2 eV, which corresponds to surface carbonaceous compounds formed during the decomposition of citric acid [53]. In [54], it is reported that the peak with 285.2 eV binding energy is related to the C-CH bond (sp<sup>3</sup> hybridization).

### 3.3. Catalytic properties of CoMoS catalysts

Catalytic properties of CoMoS/MWCNT(0.5–10% Fe<sub>2</sub>Co)@Al<sub>2</sub>O<sub>3</sub> samples in DBT hydrosulfurization and quinoline hydrodenitrogenation were tested using a model feedstock containing 1.5 wt % of DBT and 0.1 wt% of quinoline. CoMoS catalysts based on Al<sub>2</sub>O<sub>3</sub>, MWCNT, and C@Al<sub>2</sub>O<sub>3</sub> supports were studied as reference samples. CoMoS catalyst based on carbon-coated alumina (C@Al<sub>2</sub>O<sub>3</sub>) was also used as a reference sample to evaluate the effect of the carbon coating type on the formation of CoMo sulfide active component and to compare the activity with CoMoS/MWCNT(0.5–10% Fe<sub>2</sub>Co)@Al<sub>2</sub>O<sub>3</sub> catalysts in hydrotreating reactions. The C@Al<sub>2</sub>O<sub>3</sub> sample was obtained under conditions similar to the synthesis of MWCNT@Al<sub>2</sub>O<sub>3</sub> composite supports. Namely, the initial γ-Al<sub>2</sub>O<sub>3</sub> was subjected to an ethylene (200 ml/min) and argon (200 ml/min) flow at a temperature of 680 °C for 15 min. It was shown in [25] that graphitization of the alumina under these conditions provided about 30% surface coating with a layer of graphite carbon and did not significantly change the alumina morphology and textural characteristics. At the same time, it affected the morphology of the CoMo sulfide component. The preliminary modification of alumina with a layer of graphite-like carbon deposits promoted the formation of sulfide particles with a lower average slab length (2.9 vs. 3.3 nm) and a narrower distribution by stacking number with the predominance of mainly two and three-layer slabs of sulfide particles with an average stacking number of 2.4 vs. 2.1 as compared to the alumina-based sample.

The results of CoMoS/MWCNT(0.5–10% Fe<sub>2</sub>Co)@Al<sub>2</sub>O<sub>3</sub>, CoMoS/Al<sub>2</sub>O<sub>3</sub>, CoMoS/C@Al<sub>2</sub>O<sub>3</sub>, and CoMoS/MWCNT catalysts testing are presented in Table 6. According to obtained results, CoMoS/MWCNT(1.5–3% Fe<sub>2</sub>Co)@Al<sub>2</sub>O<sub>3</sub> catalysts demonstrate the highest activity in HDS and HDN reactions compared to other samples of the series. For these samples, both DBT conversion and quinoline HDN degree are about 50%, while for CoMoS/Al<sub>2</sub>O<sub>3</sub> catalyst, these values are about 30%. A further increase in the content of carbon nanotubes in MWCNT@Al<sub>2</sub>O<sub>3</sub> composite supports leads to a decrease in the HDS and HDN activity of CoMoS catalysts. According to the results of catalytic testing for all studied CoMoS samples, biphenyl (BPh) and cyclohexylbenzene (CHB) are DBT conversion products. It is well known that



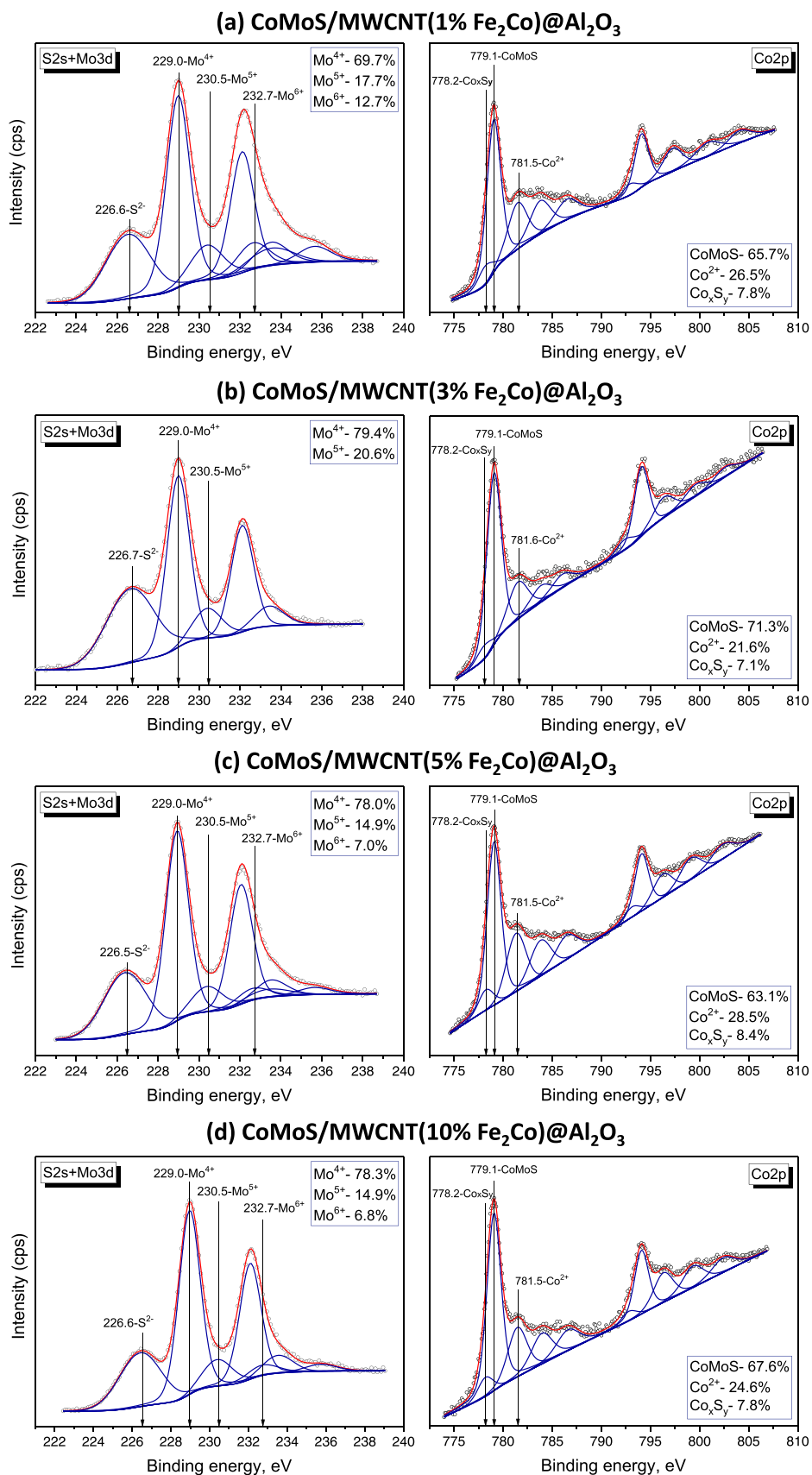


Fig. 10. S2s+Mo3d and Co2p spectra of CoMoS/MWCNT(1–10% Fe<sub>2</sub>Co)@Al<sub>2</sub>O<sub>3</sub> catalysts.

**Table 5**XPS data for CoMoS/MWCNT(1–10% Fe<sub>2</sub>Co)@Al<sub>2</sub>O<sub>3</sub> catalysts.

Parameter	CoMoS/ MWCNT (1% Fe <sub>2</sub> Co) @Al <sub>2</sub> O <sub>3</sub>	CoMoS/ MWCNT (3% Fe <sub>2</sub> Co) @Al <sub>2</sub> O <sub>3</sub>	CoMoS/ MWCNT (5% Fe <sub>2</sub> Co) @Al <sub>2</sub> O <sub>3</sub>	CoMoS/ MWCNT (10%Fe <sub>2</sub> Co) @Al <sub>2</sub> O <sub>3</sub>
Mo3d <sub>5/2</sub> , eV			229.0 ± 0.1	
Mo <sup>4+</sup> , %	69.7	79.4	78.0	78.3
Mo <sup>5+</sup> , %	17.7	20.6	14.9	14.9
Mo <sup>6+</sup> , %	12.7	0.0	7.0	6.8
Co2p <sub>3/2</sub> , eV			779.1 ± 0.1	
CoMoS, %	65.7	71.3	63.1	67.6
Co <sup>2+</sup> , %	26.5	21.6	28.5	24.6
Co <sub>x</sub> S <sub>y</sub>	7.8	7.1	8.4	7.8
Co/Mo	0.37	0.52	0.61	0.63
Al2p, eV			74.6 ± 0.1	
C1s, eV			284.5	
C/Al	5.79	26.9	56.9	87.8

**Table 6**Catalytic properties of CoMoS/MWCNT@Al<sub>2</sub>O<sub>3</sub>, CoMoS/Al<sub>2</sub>O<sub>3</sub>, CoMoS/C@Al<sub>2</sub>O<sub>3</sub>, and CoMoS/MWCNT catalysts in DBT hydrodesulfurization and quinoline hydrodenitrogenation.

Sample	DBT conversion, %	HDN degree, %	Selectivity, %	
			BPh	CHB
CoMoS/Al <sub>2</sub> O <sub>3</sub>	30.4	29.8	97.3	2.7
CoMoS/MWCNT	42.2	35.1	96.4	3.6
CoMoS/C@Al <sub>2</sub> O <sub>3</sub>	50.7	27.7	96.2	3.8
CoMoS/MWCNT(0.5% Fe <sub>2</sub> Co)@Al <sub>2</sub> O <sub>3</sub>	50.4	26.6	96.3	3.7
CoMoS/MWCNT(1% Fe <sub>2</sub> Co)@Al <sub>2</sub> O <sub>3</sub>	50.8	38.0	96.1	3.9
CoMoS/MWCNT(1.5% Fe <sub>2</sub> Co)@Al <sub>2</sub> O <sub>3</sub>	51.2	46.3	94.0	6.0
CoMoS/MWCNT(3% Fe <sub>2</sub> Co)@Al <sub>2</sub> O <sub>3</sub>	47.5	50.5	90.7	9.3
CoMoS/MWCNT(5% Fe <sub>2</sub> Co)@Al <sub>2</sub> O <sub>3</sub>	39.0	29.4	97.1	2.9
CoMoS/MWCNT(10% Fe <sub>2</sub> Co)@Al <sub>2</sub> O <sub>3</sub>	29.0	16.5	97.5	2.5

BPh – biphenyl; CHB – cyclohexylbenzene.

DBT hydrodesulfurization proceeds via two routes. The direct desulfurization (DDS) route leads to the formation of BPh. The hydrogenation (HYD) route proceeds through the preliminary saturation of one of the benzene rings with subsequent sulfur elimination and leads to the formation of CHB [27,55]. In our case, DDS is the main DBT conversion route for all studied catalysts since BPh is the main reaction product (Table 6). However, CoMoS/MWCNT(1.5% Fe<sub>2</sub>Co)@Al<sub>2</sub>O<sub>3</sub> and CoMoS/MWCNT(3% Fe<sub>2</sub>Co)@Al<sub>2</sub>O<sub>3</sub> catalysts have the highest selectivity of CHB formation, which is 6.0% and 9.3%, respectively. The latter suggests that these catalysts are characterized by an increased hydrogenation activity.

The literature suggests the concept that DDS and HYD sites of sulfide hydrotreating catalysts are different [56]. DDS occurs via perpendicular  $\sigma$  adsorption of the reacting sulfur-containing molecule, while HYD occurs via planar  $\pi$  adsorption. In this respect, the active sites at the edges and the corners of MoS<sub>2</sub> slabs can be considered as DDS and HYD sites, respectively. Taking into account the abovementioned consideration, as well as the obtained data on the morphology and the state of the sulfide component, the observed catalytic behavior of studied catalysts can be explained. As it was shown above, MWCNTs in MWCNT(1.5–3% Fe<sub>2</sub>Co)@Al<sub>2</sub>O<sub>3</sub> and MWCNT(5–10% Fe<sub>2</sub>Co)@Al<sub>2</sub>O<sub>3</sub> composite supports are characterized by different morphology (Fig. 6), structural characteristics (Fig. 7), and also defectiveness (Figs. 3–4), which affects the formation of the active component of CoMoS catalysts. Thus, in CoMoS/MWCNT(1.5–3% Fe<sub>2</sub>Co)@Al<sub>2</sub>O<sub>3</sub> catalysts, sulfide particles are formed with an average slab length of 2.6–2.7 nm, while for CoMoS/MWCNT(5–10% Fe<sub>2</sub>Co)@Al<sub>2</sub>O<sub>3</sub> catalysts the average slab length is 3.0–3.1 nm. Thus, the highest dispersion of the sulfide component is observed for CoMoS/MWCNT(1.5–3% Fe<sub>2</sub>Co)@Al<sub>2</sub>O<sub>3</sub> catalysts, which is 0.53–0.55. As a result, these catalysts have the lowest

edge-to-corner Mo atoms ratio in MoS<sub>2</sub> (Table 4). This may explain the higher activity of CoMoS/MWCNT(1.5–3% Fe<sub>2</sub>Co)@Al<sub>2</sub>O<sub>3</sub> catalysts in DBT conversion via the HYD route. Moreover, HYD activity manifests itself even in the presence of quinoline, which is known to be an inhibitor of HDS activity and strongly suppresses the HYD route [8,17]. In addition, CoMoS/MWCNT(1.5–3% Fe<sub>2</sub>Co)@Al<sub>2</sub>O<sub>3</sub> catalysts have significantly higher activity in quinoline HDN as compared to other studied samples (Table 6). It is known that HYD activity is also important for the HDN of quinoline since the conversion route involves the initial hydrogenation of the aromatic ring of the reacting nitrogen-containing molecule [57]. However, although the dispersion of the sulfide component of CoMoS/MWCNT(1.5% Fe<sub>2</sub>Co)@Al<sub>2</sub>O<sub>3</sub> and CoMoS/MWCNT(3% Fe<sub>2</sub>Co)@Al<sub>2</sub>O<sub>3</sub> catalysts is quite similar, HYD activity is significantly higher for the latter sample. The probable reason is that the ideal hexagon model is used to calculate the dispersion of MoS<sub>2</sub> particles, while the real sulfide particles in hydrotreating catalysts have a much more complex shape [2].

It should be noted that the HDS activity of CoMoS/C@Al<sub>2</sub>O<sub>3</sub> and CoMoS/MWCNT(1.5–3% Fe<sub>2</sub>Co)@Al<sub>2</sub>O<sub>3</sub> catalysts is similar. However, the HDN activity of CoMoS/MWCNT(1.5–3% Fe<sub>2</sub>Co)@Al<sub>2</sub>O<sub>3</sub> catalysts significantly exceeds the activity of CoMoS catalyst based on carbon-coated alumina (Table 6). This can be explained by the increased HYD activity of CoMoS/MWCNT(1.5–3% Fe<sub>2</sub>Co)@Al<sub>2</sub>O<sub>3</sub> catalysts due to the presence of defective MWCNTs in their structure, which are known to have the ability to adsorb hydrogen and provide good interfacial diffusion of adsorbed hydrogen from active component particles to adsorbed feedstock molecules during reaction [37]. In view of this, a properly selected and optimized structure of the carbon material in the support for CoMoS catalysts makes it possible to control their activity in hydrotreating reactions.

Thus, it was found that the most active CoMoS catalysts based on MWCNT(1.5–3% Fe<sub>2</sub>Co)@Al<sub>2</sub>O<sub>3</sub> composite supports significantly outperform CoMoS/Al<sub>2</sub>O<sub>3</sub> and CoMoS/MWCNT catalysts in HDS and HDN activity. The determining factor for this is the formation of MWCNTs on the alumina surface, which are characterized by structural defects and partially cover the alumina surface. Apparently, the fixation of MWCNTs on the alumina surface leads to blocking its strong acid sites and, thereby, prevents the strong interaction of the active component precursors with alumina during the catalyst preparation. In addition, during the impregnation, active component precursors are fixed both on the alumina surface and on defects in the inner and outer walls of MWCNTs, which also contributes to the increase of the sulfide component dispersion.

#### 4. Conclusions

A novel synthesis strategy has been developed to produce a nanostructured mesoporous MWCNT@Al<sub>2</sub>O<sub>3</sub> composite support for CoMoS hydrotreating catalysts. The proposed strategy is based on the growth of MWCNTs on alumina crystallites by ethylene CVD on the surface of preformed  $\gamma$ -Al<sub>2</sub>O<sub>3</sub> granules modified with Fe<sub>2</sub>Co alloy nanoparticles. The morphology and structural characteristics of the obtained MWCNT@Al<sub>2</sub>O<sub>3</sub> supports were tuned by varying Fe<sub>2</sub>Co content from 0.5 to 10 wt%. A comprehensive analysis of MWCNT@Al<sub>2</sub>O<sub>3</sub> supports and CoMoS/MWCNT@Al<sub>2</sub>O<sub>3</sub> catalysts using XRD, Raman spectroscopy, CHNS analysis, XRF, SEM, HRTEM, nitrogen physisorption, and X-ray photoelectron spectroscopy made it possible to establish the optimal content and structural characteristics of MWCNTs in composite supports that have a positive effect on the morphology of sulfide component. It is shown that depending on Fe<sub>2</sub>Co content, the morphology of MWCNTs in composite supports changes from single nanotubes intertwining lamellar and needle-shaped particles of the initial  $\gamma$ -Al<sub>2</sub>O<sub>3</sub> (0.5–1 wt% Fe<sub>2</sub>Co) to coils formed from intertwined individual nanotubes with inclusions of alumina particles (1.5–3 wt% Fe<sub>2</sub>Co), through strands consisting of intertwined MWCNTs covering alumina surface (5 wt% Fe<sub>2</sub>Co) to arrays of vertically oriented MWCNTs (10 wt% Fe<sub>2</sub>Co). In addition,

the synthesized MWCNT@Al<sub>2</sub>O<sub>3</sub> supports are characterized by different structural defectiveness of MWCNT, which varies depending on Fe<sub>2</sub>Co content. MWCNT(0.5–3% Fe<sub>2</sub>Co)@Al<sub>2</sub>O<sub>3</sub> supports are characterized by the highest defectiveness of MWCNTs and a shorter graphene fragment length compared to MWCNT(5–10% Fe<sub>2</sub>Co)@Al<sub>2</sub>O<sub>3</sub> and neat MWCNT. It is important to note that MWCNT(0.5–3% Fe<sub>2</sub>Co)@Al<sub>2</sub>O<sub>3</sub> and  $\gamma$ -Al<sub>2</sub>O<sub>3</sub> samples are characterized by the similar shape of pores, which indicates the uniform growth of MWCNTs on the alumina surface. Whereas MWCNT(5–10% Fe<sub>2</sub>Co)@Al<sub>2</sub>O<sub>3</sub> supports are characterized by an increase in the specific surface area, pore volume, and moisture capacity, which is associated with the generation of secondary porosity due to the formation of agglomerates of intertwined MWCNTs.

It has been established that the morphology of the support and defectiveness of MWCNTs affect the formation of sulfide component in CoMo hydrotreating catalysts. Thus, the highest dispersion of sulfide particles is characteristic of CoMoS/MWCNT(1.5% Fe<sub>2</sub>Co)@Al<sub>2</sub>O<sub>3</sub> and CoMoS/MWCNT(3% Fe<sub>2</sub>Co)@Al<sub>2</sub>O<sub>3</sub> catalysts. The morphology of MWCNT(1.5–3% Fe<sub>2</sub>Co)@Al<sub>2</sub>O<sub>3</sub> supports is represented by coils formed from intertwined individual and defective nanotubes with inclusions of initial alumina particles. Thus, the presence of alumina and defective MWCNTs fragments on the surface of the support ensures the optimal metal-support interaction, which leads to the formation of highly dispersed sulfide particles.

The activity of CoMoS/MWCNT(1.5–3% Fe<sub>2</sub>Co)@Al<sub>2</sub>O<sub>3</sub> catalysts in dibenzothiophene hydrodesulfurization and quinoline hydrodenitrogenation significantly exceeds the activity of CoMoS/Al<sub>2</sub>O<sub>3</sub> and CoMoS/MWCNT catalysts. This behavior is associated with higher MoS<sub>2</sub> dispersion and its better promotion by Co atoms resulting in higher content of the CoMoS phase in CoMoS/MWCNT(1.5–3% Fe<sub>2</sub>Co)@Al<sub>2</sub>O<sub>3</sub> catalysts. In addition, these catalysts are characterized by a higher number of HYD sites, which probably diminishes inhibition by basic nitrogen and additionally contributes to their higher activity in hydrotreating reactions.

The simple and efficient strategy for designing MWCNT@Al<sub>2</sub>O<sub>3</sub> supports for CoMo hydrotreating catalysts presented in this paper allows selective surface modification of commercially available alumina supports with carbon nanotubes and can be applied to improve the activity of conventional hydrotreating catalysts. In addition, the obtained results give new opportunities for the development and improvement of catalysts for other practically important processes by tuning the metal-support interaction.

#### CRediT authorship contribution statement

**Mariya A. Kazakova:** Conceptualization, Investigation, Writing - original draft, Visualization, Project administration, Funding acquisition. **Yulia V. Vatutina:** Investigation, Validation, Writing - review & editing. **Alexander G. Selyutin:** Investigation, Validation, Writing - review & editing. **Igor P. Prosvirin:** Investigation, Validation, Writing - review & editing. **Evgeniy Yu. Gerasimov:** Investigation. **Oleg V. Klimov:** Resources. **Alexander S. Noskov:** Supervision. **Maxim O. Kazakov:** Conceptualization, Writing - review & editing, Visualization, Supervision, Project administration.

#### Declaration of Competing Interest

The authors declare that they have no known competing financial interests or personal relationships that could have appeared to influence the work reported in this paper.

#### Data availability

The authors are unable or have chosen not to specify which data has been used.

#### Acknowledgements

The study was funded by Russian Science Foundation according to the research project № 21-73-10039, <https://rscf.ru/project/21-73-10039/>, and in part (XRF study) by the Ministry of Science and Higher Education of the Russian Federation within the state assignment for Boreskov Institute of Catalysis (project AAAA-A21-121011390054-1).

#### Appendix A. Supporting information

Supplementary data associated with this article can be found in the online version at [doi:10.1016/j.apcatb.2023.122475](https://doi.org/10.1016/j.apcatb.2023.122475).

#### References

- [1] A. Haruna, Z. Merican Aljunid Merican, S. Gani Musa, S. Abubakar, Sulfur removal technologies from fuel oil for safe and sustainable environment, *Fuel* 329 (2022), 125370.
- [2] S. Eijssbouts, L.C.A. van den Oetelaar, M. Rayner, H. Govaers, T. Boonen, Combined HR TEM and STEM-EDX evaluation – The key to better understanding of the Co-Mo sulfide active phase in real-life Co-Mo-P/Al<sub>2</sub>O<sub>3</sub> catalysts, *J. Catal.* 403 (2021) 56–73.
- [3] M. Breyse, P. Afanasiev, C. Geantet, M. Vrinat, Overview of support effects in hydrotreating catalysts, *Catal. Today* 86 (2003) 5–16.
- [4] M. Breyse, C. Geantet, P. Afanasiev, J. Blanchard, M. Vrinat, Recent studies on the preparation, activation and design of active phases and supports of hydrotreating catalysts, *Catal. Today* 130 (2008) 3–13.
- [5] S. Brunet, B. Lebeau, I. Naboulsi, L. Michelin, J.D. Comparot, C. Marichal, S. Rigolet, M. Bonne, J.-L. Blin, Effect of Mesoporous Zirconia Support on the Activity and Selectivity of 4,6-Dimethyldibenzothiophene Hydrodesulfurization, *Catalysts* 10 (2020) 1162.
- [6] T. Roy, J. Rousseau, A. Daudin, G. Pirngruber, B. Lebeau, J.-L. Blin, S. Brunet, Deep hydrodesulfurization of 4,6-dimethyldibenzothiophene over CoMoS/TiO<sub>2</sub> catalysts: Impact of the TiO<sub>2</sub> treatment, *Catal. Today* 377 (2021) 17–25.
- [7] R. Cattaneo, T. Shido, R. Prins, The Relationship between the Structure of NiMo/SiO<sub>2</sub> Catalyst Precursors Prepared in the Presence of Chelating Ligands and the Hydrodesulfurization Activity of the Final Sulfided Catalysts, *J. Catal.* 185 (1999) 199–212.
- [8] T.A. Zepeda, B. Pawelec, R. Obeso-Estrella, J.N. Díaz de León, S. Fuentes, G. Alonso-Núñez, J.L.G. Fierro, Competitive HDS and HDN reactions over NiMoS/HMS-Al catalysts: Diminishing of the inhibition of HDS reaction by support modification with P, *Appl. Catal. B: Environ.* 180 (2016) 569–579.
- [9] L. Kaluza, J. Karban, D. Gulková, Activity and selectivity of Co(Ni)Mo sulfides supported on MgO, Al<sub>2</sub>O<sub>3</sub>, ZrO<sub>2</sub>, TiO<sub>2</sub>, MCM-41 and activated carbon in parallel hydrodeoxygenation of octanoic acid and hydrodesulfurization of 1-benzothiophene, *React. Kinet. Mech. Catal.* 127 (2019) 887–902.
- [10] W. Zhou, Q. Wei, Y. Zhou, M. Liu, S. Ding, Q. Yang, Hydrodesulfurization of 4,6-dimethyldibenzothiophene over NiMo sulfide catalysts supported on meso-microporous Y zeolite with different mesopore sizes, *Appl. Catal. B: Environ.* 238 (2018) 212–224.
- [11] M. Hussain, J.S. Yun, S.-K. Ihm, N. Russo, F. Geobaldo, Synthesis, Characterization, and Thiophene Hydrodesulfurization Activity of Novel Macroporous and Mesoporous Carbon, *Ind. Eng. Chem. Res.* 50 (2011) 2530–2535.
- [12] C. Jang, J. Ji, J. Yu, Applicability of CNT as support candidate for thiophene hydrodesulfurization and 1-octene hydrogenation catalyst, *Inorg. Chem. Commun.* 129 (2021), 108615.
- [13] M.O. Kazakov, M.A. Kazakova, Y.V. Vatutina, T.V. Larina, Y.A. Chesalov, E. Y. Gerasimov, I.P. Prosvirin, O.V. Klimov, A.S. Noskov, Comparative study of MWCNT and alumina supported CoMo hydrotreating catalysts prepared with citric acid as chelating agent, *Catal. Today* 357 (2020) 221–230.
- [14] Y.V. Vatutina, M.A. Kazakova, E.Y. Gerasimov, I.P. Prosvirin, O.V. Klimov, A. S. Noskov, M.O. Kazakov, Effect of Organic Additives on the Structure and Hydrotreating Activity of a CoMoS/Multiwalled Carbon Nanotube Catalyst, *Ind. Eng. Chem. Res.* 59 (2020) 20612–20623.
- [15] J.L. Pinilla, H. Purón, D. Torres, S. de Llobet, R. Moliner, I. Suelves, M. Millan, Carbon nanofibres coated with Ni decorated MoS<sub>2</sub> nanosheets as catalyst for vacuum residue hydroprocessing, *Appl. Catal. B: Environ.* 148–149 (2014) 357–365.
- [16] Z. Hajjar, M. Kazemeini, A. Rashidi, S. Soltanali, Hydrodesulfurization catalysts based on carbon nanostructures: A review, *Fuller. Nanotub. Carbon Nanostruct.* 26 (2018) 557–569.
- [17] H. Topsøe, The role of Co–Mo–S type structures in hydrotreating catalysts, *Appl. Catal. A: Gen.* 322 (2007) 3–8.
- [18] I. Vázquez-Garrido, A. López-Benítez, G. Berhault, A. Guevara-Lara, Effect of support on the acidity of NiMo/Al<sub>2</sub>O<sub>3</sub>-MgO and NiMo/TiO<sub>2</sub>-Al<sub>2</sub>O<sub>3</sub> catalysts and on the resulting competitive hydrodesulfurization/hydrodenitrogenation reactions, *Fuel* 236 (2019) 55–64.
- [19] J. Xu, T. Huang, Y. Fan, Highly efficient NiMo/SiO<sub>2</sub>-Al<sub>2</sub>O<sub>3</sub> hydrodesulfurization catalyst prepared from gemini surfactant-dispersed Mo precursor, *Appl. Catal. B: Environ.* 203 (2017) 839–850.

- [20] P. Afanasiev, Mixed  $\text{TiO}_2$ - $\text{ZrO}_2$  support for hydrotreating, obtained by co-precipitation from Zr basic carbonate and Ti oxosulfate, *Catal. Commun.* 9 (2008) 734–739.
- [21] Q. Wei, Y. Li, T. Zhang, X. Tao, Y. Zhou, K. Chung, C. Xu,  $\text{TiO}_2$ - $\text{SiO}_2$ -Composite-Supported Catalysts for Residue Fluid Catalytic Cracking Diesel Hydrotreating, *Energy Fuels* 28 (2014) 7343–7351.
- [22] A.P. Glotov, A.V. Vutolkina, N.A. Vinogradov, A.A. Pimerzin, V.A. Vinokurov, A. A. Pimerzin, Enhanced HDS and HYD activity of sulfide Co-PMo catalyst supported on alumina and structured mesoporous silica composite, *Catal. Today* 377 (2021) 82–91.
- [23] A.E. Cruz Pérez, Y. Torrez Jiménez, J.J. Velasco Alejo, T.A. Zepeda, D.M. Frías Márquez, M.G. Rivera Ruedas, S. Fuentes, J.N. Díaz de León, NiW/MgO- $\text{TiO}_2$  catalysts for dibenzothiophene hydrodesulfurization: Effect of preparation method, *Catal. Today* 271 (2016) 28–34.
- [24] M.E. Cervantes-Gaxiola, M. Arroyo-Albiter, R. Maya-Yescas, J.L. Rico-Cerda, A. Guevara-Lara, J. Espino-Valencia, Synthesis, characterization and catalytic activity during hydrodesulfurization of dibenzothiophene of NiMoW catalysts supported on AlTi mixed oxides modified with MgO, *Fuel* 100 (2012) 57–65.
- [25] M.A. Kazakova, Y.V. Vatutina, I.P. Prosvirin, E.Y. Gerasimov, A.V. Shuvaev, O. V. Klimov, A.S. Noskov, M.O. Kazakov, Boosting hydrodesulfurization activity of CoMo/ $\text{Al}_2\text{O}_3$  catalyst via selective graphitization of alumina surface, *Micro Mesopor. Mat.* 317 (2021), 111008.
- [26] Y. Xu, P. Li, S. Yuan, B. Sui, W. Lai, X. Yi, W. Fang, Sacrificial carbonaceous coating over alumina supported Ni-MoS<sub>2</sub> catalyst for hydrodesulfurization, *RSC Adv.* 9 (2019) 11951–11959.
- [27] L. Li, M. Wang, L. Huang, X. Liu, X. Zhang, H. Sun, Q. Yu, F. Yang, Q. Guo, B. Shen, Electron-donating-accepting behavior between nitrogen-doped carbon materials and Fe species and its promotion for DBT hydrodesulfurization, *Appl. Catal. B: Environ.* 254 (2019) 360–370.
- [28] S.A. Al-Hammadi, A.M. Al-Amer, T.A. Saleh, Alumina-carbon nanofiber composite as a support for MoCo catalysts in hydrodesulfurization reactions, *Chem. Eng. J.* 345 (2018) 242–251.
- [29] T.A. Saleh, S.A. Al-Hammadi, A novel catalyst of nickel-loaded graphene decorated on molybdenum-alumina for the HDS of liquid fuels, *Chem. Eng. J.* 406 (2021), 125167.
- [30] T.A. Saleh, Carbon nanotube-incorporated alumina as a support for MoNi catalysts for the efficient hydrodesulfurization of thiophenes, *Chem. Eng. J.* 404 (2021), 126987.
- [31] T.A. Saleh, K.O. Sulaiman, S.A. Al-Hammadi, Effect of carbon on the hydrodesulfurization activity of MoCo catalysts supported on zeolite/active carbon hybrid supports, *Appl. Catal. B: Environ.* 263 (2020), 117661.
- [32] I. Ali, A.A. Al-Arfaj, T.A. Saleh, Carbon nanofiber-doped zeolite as support for molybdenum based catalysts for enhanced hydrodesulfurization of dibenzothiophene, *J. Mol. Liq.* 304 (2020), 112376.
- [33] A. Magrez, J.W. Seo, R. Smajda, M. Mionić, L. Forró, Catalytic CVD Synthesis of Carbon Nanotubes: Towards High Yield and Low Temperature Growth, *Materials* 3 (2010) 4871–4891.
- [34] Y. Yan, J. Miao, Z. Yang, F.-X. Xiao, H.B. Yang, B. Liu, Y. Yang, Carbon nanotube catalysts: recent advances in synthesis, characterization and applications, *Chem. Soc. Rev.* 44 (2015) 3295–3346.
- [35] M.A. Kazakova, A. Koul, G.V. Golubtsov, A.G. Selyutin, A.V. Ishchenko, R.I. Kvon, B.A. Kolesov, W. Schuhmann, D.M. Morales, Nitrogen and Oxygen Functionalization of Multi-Walled Carbon Nanotubes for Tuning the Bifunctional Oxygen Reduction/Oxygen Evolution Performance of Supported FeCo Oxide Nanoparticles, *ChemElectroChem* 8 (2021) 2803–2816.
- [36] T.C. Ho, L. Qiao, Competitive adsorption of nitrogen species in HDS: Kinetic characterization of hydrogenation and hydrogenolysis sites, *J. Catal.* 269 (2010) 291–301.
- [37] I.C. Gerber, P. Serp, A Theory/Experience Description of Support Effects in Carbon-Supported Catalysts, *Chem. Rev.* 120 (2020) 1250–1349.
- [38] A.S. Andreev, D.V. Krasnikov, V.I. Zaikovskii, S.V. Cherepanova, M.A. Kazakova, O.B. Lapina, V.L. Kuznetsov, J.B. d'Espinose de Lacaillerie, Internal field  $^{59}\text{Co}$  NMR study of cobalt-iron nanoparticles during the activation of  $\text{CoFe}_2/\text{CaO}$  catalyst for carbon nanotube synthesis, *J. Catal.* 358 (2018) 62–70.
- [39] G.V. Golubtsov, M.A. Kazakova, A.G. Selyutin, A.V. Ishchenko, V.L. Kuznetsov, Mono-, Bi-, and Trimetallic Catalysts for the Synthesis of Multiwalled Carbon Nanotubes Based on Iron Subgroup Metals, *J. Struct. Chem.* 61 (2020) 640–651.
- [40] A.A. Zhdanov, M.A. Kazakova, Use of carbon materials with various nature in determining the content of metals in carbon nanotubes by the X-ray fluorescence method, *J. Anal. Chem.* 75 (2020) 312–319.
- [41] S. Kasztelan, H. Toulhoat, J. Grimblot, J.P. Bonnelle, A geometrical model of the active phase of hydrotreating catalysts, *Appl. Catal.* 13 (1984) 127–159.
- [42] M. Thommes, K. Kaneko, A.V. Neimark, J.P. Olivier, F. Rodriguez-Reinoso, J. Rouquerol, K.S.W. Sing, Physisorption of gases, with special reference to the evaluation of surface area and pore size distribution (IUPAC Technical Report), *Pure Appl. Chem.* 87 (2015) 1051–1069.
- [43] W.E. Mahmoud, F.S. Al-Hazmi, G.H. Al-Harbi, Wall by wall controllable unzipping of MWCNTs via intercalation with oxalic acid to produce multilayers graphene oxide ribbon, *Chem. Eng. J.* 281 (2015) 192–198.
- [44] M.A. Kazakova, A.G. Selyutin, M.V. Parfenov, A.V. Ishchenko, M.O. Kazakov, Graphitization of alumina as a way to stabilize its textural characteristics under hydrothermal conditions, *Micro Mesopor. Mat.* 341 (2022), 112038.
- [45] A. Sadezky, H. Muckenhuber, H. Grothe, R. Niessner, U. Pöschl, Raman microspectroscopy of soot and related carbonaceous materials: Spectral analysis and structural information, *Carbon* 43 (2005) 1731–1742.
- [46] C. Mapelli, C. Castiglioni, G. Zerbi, K. Müllen, Common force field for graphite and polycyclic aromatic hydrocarbons, *Phys. Rev. B* 60 (1999) 12710–12725.
- [47] B. Dippel, H. Jander, J. Heintzenberg, NIR FT Raman spectroscopic study of flame soot, *Phys. Chem. Chem. Phys.* 1 (1999) 4707–4712.
- [48] A. Cuesta, P. Dhamelincourt, J. Laureys, A. Martínez-Alonso, J.M.D. Tascón, Raman microprobe studies on carbon materials, *Carbon* 32 (1994) 1523–1532.
- [49] S. Eijssbouts, J.J.L. Heinerma, H.J.W. Elzerman, MoS<sub>2</sub> structures in high-activity hydrotreating catalysts: I. Semi-quantitative method for evaluation of transmission electron microscopy results. Correlations between hydrodesulfurization and hydrodenitrogenation activities and MoS<sub>2</sub> dispersion, *Appl. Catal. A: Gen.* 105 (1993) 53–68.
- [50] I. Alstrup, I. Chorkendorff, R. Candia, B.S. Clausen, H. Topsøe, A combined X-Ray photoelectron and Mössbauer emission spectroscopy study of the state of cobalt in sulfided, supported, and unsupported Co-Mo catalysts, *J. Catal.* 77 (1982) 397–409.
- [51] H.-Y. Shang, C.-G. Liu, R.-Y. Zhao, M.-B. Wu, F. Wei, XPS characterization of carbon nanotube supported CoMo hydrodesulfurization catalysts, *Chin. J. Chem.* 22 (2004) 1250–1256.
- [52] R.H. Bradley, K. Cassidy, R. Andrews, M. Meier, S. Osbeck, A. Andreu, C. Johnston, A. Crossley, Surface studies of hydroxylated multi-wall carbon nanotubes, *Appl. Surf. Sci.* 258 (2012) 4835–4843.
- [53] A.V. Pashigreva, O.V. Klimov, G.A. Bukhtiyarova, M.A. Fedotov, D.I. Kochubey, Y. A. Chesalov, V.I. Zaikovskii, I.P. Prosvirin, A.S. Noskov, The superior activity of the CoMo hydrotreating catalysts, prepared using citric acid: what's the reason? *Stud. Surf. Sci. Catal.* (2010) 109–116.
- [54] J. Díaz, G. Paolicelli, S. Ferrer, F. Comin, Separation of the sp<sup>3</sup> and sp<sup>2</sup> components in the C1s photoemission spectra of amorphous carbon films, *Phys. Rev. B* 54 (1996) 8064–8069.
- [55] D. Gao, A. Duan, X. Zhang, Z. Zhao, H.E.J. Li, H. Wang, Synthesis of NiMo catalysts supported on mesoporous Al-SBA-15 with different morphologies and their catalytic performance of DBT HDS, *Appl. Catal. B: Environ.* 165 (2015) 269–284.
- [56] M. Egorova, R. Prins, The role of Ni and Co promoters in the simultaneous HDS of dibenzothiophene and HDN of amines over Mo/ $\gamma$ - $\text{Al}_2\text{O}_3$  catalysts, *J. Catal.* 241 (2006) 162–172.
- [57] S. Albersberger, H. Shi, M. Wagenhofer, J. Han, O.Y. Gutiérrez, J.A. Lercher, On the enhanced catalytic activity of acid-treated, trimetallic Ni-Mo-W sulfides for quinoline hydrodenitrogenation, *J. Catal.* 380 (2019) 332–342.